Prolonged Crowding Initiates Tumor Invasion with Mechanomemory by Pressure-Sensation of Membrane Domains

Xinbin Zhao[1, 9], Min Tan[2, 9], Long Li[3, 9], Xubo Lin[1], Zekun Li[4], Xiaohuan Wang[5], Bingqi Song[2], Zheng Guo[2], Tailin Chen[6], Sen Hou[2], Jiehou Fan[7], Shijiang Wang[8], Yun Zhang[4] *, Yubo Fan[1,2] * and Jing Du[2] *

[1]Beijing Advanced Innovation Center for Biomedical Engineering, School of Engineering Medicine, Beihang University; Beijing, 100191, China

[2]Beijing Advanced Innovation Center for Biomedical Engineering, School of Biological Science and Medical Engineering, Beihang University; Beijing, 100191, China

[3]State Key Laboratory of Nonlinear Mechanics and Beijing Key Laboratory of Engineered Construction and Mechanobiology, Institute of Mechanics, Chinese Academy of Sciences, Beijing 100190, China; Center of Materials Science and Optoelectronics Engineering, University of Chinese Academy of Sciences; Beijing, 100049, China

[4]State Key Laboratory of Molecular Oncology, National Cancer Center/National Clinical Research Center for Cancer/Cancer Hospital, Chinese Academy of Medical Sciences and Peking Union Medical College; Beijing, 100021, China

[5]Department of Rehabilitation Medicine, Peking University Third Hospital; Beijing, 100191, China.

[6]School of Basic Medicine, Guangxi University of Chinese Medicine; Nanning, 530200, China

[7]Department of Breast Surgery, Second People's Hospital of Dezhou; Beijing, 253000, China

[8]Department of Radiation Oncology, Shandong Cancer Hospital and Institute, Shandong First Medical University, Shandong Academy of Medical Sciences; Jinan, 250117, China

[9]These authors contributed equally

*Corresponding author. Email: Correspondence: yunzhang@cicams.ac.cn (Y.Z.), yubofan@buaa.edu.cn (YB.F.), dujing@buaa.edu.cn (J.D.)

Key words: prolonged crowding; invasion initiation; mechanomemory; Laplace pressure；membrane domains

ABSTRACT

During the progression from epithelial neoplasms to invasive carcinoma, cells are subjected to prolonged confinement. However, the response of cancer cells to such mild yet sustained compressive pressure during the initial stages of tumor invasion remain poorly understood. Here, using a spontaneous crowding model to recapitulate the progressive compressive stress caused by cell proliferation, we demonstrated that prolonged crowding alone is sufficient to induce the acquisition of an invasive phenotype and associated gene expression patterns in cancer cells. This invasiveness persisted even after cells were removed from the crowded environment, a phenomenon mediated by mechanomemory. By combining genetic manipulations, mechanical modeling, and biophysical measurements, we revealed that the disaggregation of membrane domains—driven by a nanoscale smooth-corrugated topography transition of plasma membranes induced by Laplace pressure under crowded conditions—is essential for initiating cancer cell invasion. Inhibiting membrane domains disaggregation through membrane-to-cortex-attachment effectively suppresses cancer cell invasion in both cellular crowding models and mouse xenograft models. This study underscores the critical role of tissue-scale mechanics in regulating the biophysics of mechanosensitive membrane domains during the early stages of tumor invasion.

INTRODUCTION

Mechanical force modulates embryonic development, influences tissue homeostasis, and contributes to the development of many diseases including cancer[1-3]. The primary tumor microenvironment (TME) is characterized by a diverse array of harsh mechanical cues, including increased matrix stiffness and solid stress[4]. Due to cell growth and surrounding pressures, solid stress is the force transmitted through the elastic solid phase of the tissue and can generate tensile stress and compressive stress[5]. During the development from epithelial neoplasms to invasive carcinoma, uncontrolled growth and proliferation of cancer cells pushes and displaces the surrounding normal tissue, which in turn constrains tumor expansion and results in crowded tissues and generates compressive mechanical stress within solid tumor and surrounding extracellular matrix (ECM)[6-8].

Recent studies in mouse models of skin tumor reveal that constraining forces from overlying suprabasal cancer cells and underlying ECM shape tissue architecture and affect tumor invasion[9,10]. Strong confinement has been shown to drive a fast amoeboid migration in mesenchymal cells and embryonic progenitor cells[11,12]. The cell nucleus is able to sense constraining forces and responds to them by switching to a rapid migratory phenotypic state that enables cancer cells to squeeze out from compressive conditions[13,14]. Strong confinement during cell invasion also causes nuclear deformation, which results in localized nuclear envelope rupture and DNA damage, and promotes invasive phenotype of MCF10DCIS.com cells[15]. At present, experimental methods used to study the invasion of cancer cells in response to physical confinement mainly subject cells to transient and strong force by *in vitro* compression device or microfabricated duct-on-a-chip which mimicked the invasive process *per se* of cancer cells through a narrow channel[15,16]. However, the mechanical adaptability of cancer cells to the mild and prolonged compression under crowded conditions and their function in the initiation of tumor invasion remain unclear.

Emerging evidence has revealed the ability of cells to remember the mechanical stimuli after the cessation of force, which is termed “mechanomemory”[17]. Mechanomemory has been studied in mesenchymal stem cells and epithelial cells, mostly with high matrix stiffness as a physical stimulus. However, the investigation of cell mechanomemory in the cancer field is currently in its infancy[18,19]. Whether prolonged exposure to compressive stress in the crowded TME could imprint this mechanomemory in cancer cells has not been studied.

In this study, we found that prolonged crowding initiates invasion with mechanomemory in cancer cells by using a spontaneous crowding model composed of a freely growing monoclonal cell sheet. Combining genetic manipulations, biophysical measurements, and mechanical modeling, we revealed that the disaggregation of membrane domains sensitive to prolonged crowding drives cancer cell invasiveness. Membrane domains disaggregation is induced by a nanoscale smooth-corrugated topography transition (nSCTT) of plasma membranes under Laplace pressure. Finally, we demonstrated that enhancing the aggregation of membrane domains by suppressing the nSCTT through membrane-to-cortex-attachment (MCA) inhibits cancer cell invasiveness in cellular crowding models and mouse xenograft models.

RESULTS

Prolonged crowding initiates cancer cell invasion

To investigate the role of prolonged crowding in tumor invasion, we employed a spontaneous crowding model[20] using HeLa cells, which were allowed to freely grow as a monoclonal cell sheet for 14 days (Fig. 1a). According to our previous study, this cell sheet spontaneously developed a progressive crowding gradient radiating from the central region to the periphery driven by interfacial shear stress between the cell sheet and the ECM[21]. The extent of crowding was quantified using a metric termed "crowding strain", calculated as $(A_0 - A_n)/A_0$, where A_0 represents the nuclear area of cells in sparse culture, and A_n denotes the nuclear area of cells within the cell sheet (Fig. 1b). Based on crowding strain values, the cell sheet was segmented into two regions: an uncrowded region (crowding strain ranging from -0.3 to 0) and a crowded region (crowding strain from 0 to 0.3) (Fig. 1c). Using this model, cells in the crowded region were subjected to long-term compressive stress induced by prolonged crowding for 7-14 days. Transwell invasion assays revealed that crowded cells exhibited significantly enhanced invasiveness compared to uncrowded cells (Fig. 1d and e). These findings were corroborated in other cancer cell lines, including MC38 (a murine colorectal cancer cell line) and A431 (a human skin cancer cell line) (Fig. 1d and e). Furthermore, time-lapse imaging of NLS-GFP$^+$ HeLa cell sheets demonstrated that cell invasiveness originated predominantly from crowded regions (Fig. S1a and b), providing direct evidence that prolonged crowding initiates cancer cell invasion.

Given that the invasion process is known to require degradation of the surrounding ECM[22], we next investigated whether prolonged crowding influences ECM degradation. To this end, we utilized Cy5-conjugated gelatin hydrogels coated on culture dishes. Vertical cross-sectional (XZ-plane) imaging revealed that the thickness of the ECM gradually decreased with increasing crowding strain (Fig. S1c and d), demonstrating that prolonged crowding enhances the capacity of HeLa cells to degrade the ECM. Furthermore, immunofluorescence staining of cortactin, an actin-bundling protein enriched in invadopodia of tumor cells[23,24], showed that the number of invadopodia per cell progressively increased with higher crowding strain in HeLa cells cultured on matrigel-coated culture dishes (Fig. S1e and f). Taken together, these results suggest that prolonged crowding is sufficient to drive the initiation of cancer cell invasion.

115

116 **Prolonged crowding-initiated cancer cell invasion is retained via mechanomemory**

117 Recent studies have demonstrated the ability of matrix stiffness to imprint mechanomemory onto the
118 cells after cessation of a force[25,26]. We next investigated whether cells exposed to prolonged
119 crowding retain their invasive properties after leaving crowded regions. HeLa cells were first
120 cultured under crowded or uncrowded conditions for varying durations (priming time). These primed
121 cells were then transferred to sparse culture conditions (crowding strain ≈ 0) for different periods
122 (memory time) before being subjected to invasion assays, such as Transwell assay (Fig. 1f). Cells
123 primed in crowded cultures for 3 and 5 days exhibited significantly elevated invasiveness compared
124 to those primed for 1 and 2 days (Fig. 1g and h). Furthermore, cells primed for 5 days displayed
125 greater invasiveness than those primed for 3 days (Fig. 1h), indicating a priming-time-dependent
126 mechanomemory that governs the retention of invasiveness.

127 We next investigated the duration of crowding-induced mechanomemory by priming cells for 5
128 days in crowded or uncrowded cultures, followed by transfer to sparse culture for 1, 2, 3, or 7 days
129 (Fig. 1i). Transwell invasion assays revealed that crowded cells retained significantly higher
130 invasiveness compared to uncrowded cells after 1 and 2 days of sparse culture (Fig. 1i and j). To
131 further explore the relationship between priming duration and mechanomemory, we extended the
132 priming time in crowded cultures up to 20 days. Transwell assays demonstrated that the duration of
133 mechanomemory increased with priming time, with cells primed for 20 days retaining enhanced
134 invasiveness even after 7 days in sparse culture (Fig. 1k). This retention of invasiveness via
135 mechanomemory was consistently observed in A431 cells (Fig. S2). Additionally, crowding-primed
136 cells (5 days) exhibited a significantly higher number of invadopodia per cell compared to
137 uncrowded cells after 1, 2, and 3 days in sparse culture (Fig. 1l and m). Notably, mechanomemory
138 was also evident in the ECM degradation ability of crowding-primed cells (Fig. 1n and o). Together,
139 these results demonstrate that prolonged crowding not only initiates cancer cell invasion but also
140 imprints a duration-dependent mechanomemory, sustaining the invasive phenotype even after the
141 removal of crowding stress.

142 To further characterize gene expression regulated by prolonged crowding, we performed RNA
143 sequencing of crowding-primed cells (20 days) followed by sparse culture for varying durations (0, 1,

3, or 10 days). We identified 1,990 up-regulated and 1,408 down-regulated genes that were significantly altered in crowded cells compared to uncrowded cells without a sparse culture step (Fig. 1p). Among these, genes involved in ECM degradation, such as *MMP28*, *MMP14, ADAM9,* and *ADAM10*[27], as well as *RAB5A*, as a micro-invasive marker, were upregulated in crowded cells compared to uncrowded cells (Fig. 1q). These findings align with the enhanced invasiveness observed in crowded cells.

Additionally, we detected significantly elevated levels of epithelial-mesenchymal transition (EMT)-inducing transcription factors, including *SNAIL* and *ZEB1*, in crowded cells (Fig. 1q), indicating a transition towards a more mesenchymal-like state. Notably, the increased expression levels of *MMP14, MMP28*, and *SNAIL* in crowded cells were sustained for at least 3 days in sparse cultures (Fig. 1r), consistent with the retention of mechanomemory. These results demonstrate that prolonged crowding enhances the expression of genes associated with invasiveness and retains these expression patterns through mechanomemory. Collectively, these findings establish that prolonged crowding not only initiates cancer cell invasion but also imprints a mechanical memory that sustains the invasive phenotype even after the removal of crowding stress.

Prolonged crowding initiates cancer cell invasion by disrupting the aggregation of membrane domains

To elucidate the mechanism underlying the invasion initiated by prolonged crowding, we further analyzed RNA-seq data and correlated gene expression changes with memory time using mFuzz. Our analysis identified 187 genes in Cluster 2 whose expression trends correlated with memory time, showing a recovery in crowded cells after 1, 3, and 10 days of sparse culture compared to uncrowded cells (Fig. S3). Gene Ontology (GO) cellular component enrichment analysis of Cluster 2 genes revealed that most were associated with the cell membrane or membrane domains (Fig. 2a). Previous studies have established that plasma membranes contain numerous lipid microdomains enriched in cholesterol and sphingolipids[28,29]. These microdomains, termed lipid rafts, include subtypes such as flotillin-rich planar lipid rafts and caveolin-rich caveolae[28]. Lipid rafts play critical roles in various physiological and pathological processes by aggregating into larger platforms that regulate signaling

173 regulation[28-30]. To experimentally assess whether membrane domains are affected by prolonged
174 crowding, we monitored the abundance of membrane domains in the cellular crowding model using
175 Cy5-conjugated cholera toxin subunit B (CTxB), which specifically binds to ganglioside GM1, a
176 common ganglioside enriched in membrane domains[31]. Fluorescence imaging revealed that the
177 extent of CTxB-labeled membrane domains at the apical plasma membrane was significantly
178 reduced in crowded cells compared to uncrowded cells (Fig. 2b and c). Specifically, both the
179 fluorescence intensity of CTxB and the number of CTxB clusters at the apical plasma membrane per
180 cell exhibited a crowding-strain-dependent reduction when the crowding strain exceeded 0 (Fig.
181 2d-f). Further, immunofluorescence staining against Flotillin-1, Caveolin-1, and Cavin-1 also
182 showed significant crowding-strain-dependent decreases in signal intensity (Fig. 2g-j and Fig. S4).
183 These results demonstrate that the aggregation of membrane domains at the apical plasma membrane
184 in cancer cells is disrupted by prolonged crowding.

185 To investigate whether the disrupted aggregation of membrane domains contributes to initiation of
186 cancer cell invasion under prolonged crowding, we modulated membrane domains by enriching or
187 depleting membrane cholesterol content. This was achieved through the addition of exogenous
188 cholesterol or methyl-β-cyclodextrin (MβCD)[32], respectively, in the cellular crowding model.
189 Transwell invasion assays revealed that cholesterol enrichment significantly inhibited cell invasion
190 compared to the control group, whereas cholesterol depletion by MβCD significantly enhanced the
191 invasiveness in crowded cells (Fig. 2k, l). Notably, both exogenous cholesterol addition and MβCD
192 treatment reduced the difference in invasiveness between crowded and uncrowded cells (Fig. 2l).
193 Furthermore, exogenous cholesterol addition decreased the number of invadopodia per cell, while
194 MβCD treatment increased it, effectively eliminating the difference between crowded and
195 uncrowded cells (Fig. 2m, n). These findings collectively demonstrate that prolonged crowding
196 initiates cancer cell invasion by disrupting the aggregation of membrane domains.

197 Extensive studies have established a strong link between carcinoma invasion and the loss of
198 epithelial integrity, particularly through the disruption of cell-cell contacts[33]. Cholesterol-rich
199 membrane domains at apical junctions are known to be essential for tight junction formation[34]. In our
200 study, using an antibody against claudin-1, a key component of tight junction[35], we observed a
201 progressive decline in tight junction integrity as crowding strain increased in the cellular crowding
202 model (Fig. 2o, p). Furthermore, the fluorescence intensity of CTxB, which labels membrane

203 domains, showed a positively correlated with Claudin-1 intensity (Fig. 2o, p). These results indicate
204 that prolonged crowding initiates cancer cell invasion by disrupting epithelial integrity, a process
205 mediated by the disaggregation of membrane domains.

206 Numerous studies have shown that PI3K/AKT and MAPK/ERK pathways are associated with
207 tumor progression such as invasion and display activating genetic alterations in more than 40% of
208 primary tumors[36-38]. Next, we wondered whether these pathways participate in tumor invasion
209 initiated by prolonged crowding. Immunofluorescence staining revealed that the phosphorylation of
210 Akt and ERK was significantly upregulated in crowded cells versus uncrowded cells, implying that
211 prolonged crowding activated these signaling pathways (Fig. 2q-t). Together, these findings
212 demonstrate that the activation of Akt and ERK , triggered by prolonged crowding, is implicated in
213 the the initiation of cancer cell invasion.

214

215

216 **Prolonged crowding triggers a nanoscale smooth-corrugated topography transition of plasma**
217 **membranes**

218 Given that membrane domain availability is regulated by lipid metabolism, we next evaluated the
219 levels of cholesterol and GM1 ganglioside in cells exposed to prolonged crowding[28,31]. However,
220 fluorescent filipin III staining revealed no significant differences in free cholesterol levels between
221 uncrowded cells and crowded cells (Fig. S5a, b). Similarly, immunofluorescence staining using an
222 antibody against GM1 ganglioside indicated that its levels at the apical plasma membrane remained
223 unchanged under different crowding strains (Fig. S5c, d). These findings suggest that prolonged
224 crowding does not significantly alter the levels of main components of membrane domains.

225 Recent studies reported that the topographic configuration of cellular membranes plays a critical
226 role in regulating membrane domains[39]. To further investigate the mechanism underlying the
227 disaggregation of membrane domains, we first analyzed the topology of plasma membranes. In the
228 cellular crowding model, we observed significant deformation of plasma membranes in crowded
229 cells compared to uncrowded cells (Fig. 3a and b). Furthermore, the intensity of CTxB-labeled
230 membrane domains at the apical plasma membrane progressively decreased as membrane curvature
231 increased (Fig. 3c). We further examined plasma membrane topology in a subcutaneous nude mouse

232 xenograft model using EYFP-mem$^+$ HeLa cells. This revealed pronounced plasma membrane
233 deformation in cells within micro-invasive foci exposed to crowding (Fig. 3d-f). Consistent plasma
234 membrane deformation was also observed in human skin cancer tissue (Fig. 3g, h), as well as in
235 cervical and breast cancer tissues (Fig. S6). These results demonstrate that severe plasma membrane
236 deformation, associated with membrane domain disaggregation, occurs in cells exposed to crowded
237 conditions.

238 To further assess the effects of prolonged crowding on membrane deformation, we analyzed the
239 surface topography of plasma membranes in EYFP-mem$^+$ HeLa cells subjected to prolonged
240 crowding. 3D confocal imaging revealed that the apical plasma membrane of crowded cells exhibited
241 enhanced nanoscale protrusions, in contrast to the much smoother topography observed in
242 uncrowded cells (Fig. 3i, j). This indicates a nanoscale topography transition of plasma membranes
243 from a smooth to a corrugated state, induced by prolonged crowding. To further characterize this
244 transition, we employed scanning electron microscopy (SEM), transmission electron microscopy
245 (TEM), and atomic force microscopy (AFM). SEM and TEM imaging confirmed an enrichment of
246 nanoscale protrusions at the apical plasma membrane in crowded cells compared to uncrowded cells
247 (Fig. 3k-m). AFM analysis demonstrated that the average roughness (Ra), root mean square
248 roughness (Rq), and cellular height were all significantly increased in crowded cells (Fig. 3n, o and
249 Fig. S7a, b). Notably, consistent with the memory retention of invasiveness in cells primed by
250 prolonged crowding, cells primed in crowding culture for 5 days retained elevated cell protrusions
251 (*e.g.*, filopodia) even after 3 days of sparse culture, compared to uncrowded cells (Fig. 3p-r). Taken
252 together, these results demonstrate that prolonged crowding triggers a nanoscale smooth-corrugated
253 topography transition (nSCTT) in plasma membranes, providing a mechanistic basis for the
254 disaggregation of membrane domains and invasion initiation.

255

256

257 **Prolonged crowding increases Laplace pressure to disrupt the aggregation of membrane**
258 **domains**

259 To investigate the mechanism underlying the nSCTT of plasma membranes triggered by prolonged
260 crowding, we next measured the tension of plasma membranes, which is known to remodel

261 membrane topography by controlling the assembly of curvature-generating proteins[40]. By analyzing
262 the lifetime of a live-cell fluorescent membrane tension probe, Flipper-TR[41], we found that the
263 tension of the apical plasma membrane in cells exposed to prolonged crowding was significantly
264 reduced compared to that in uncrowded cells (Fig. 4a, b). Plasma membrane tension is known to
265 depend on the contractility of cortical actin[42]. By fluorescence resonance energy transfer
266 (FRET)-based biosensors[43], we further analyzed the activity of Rho GTPases, which are master
267 regulators of actomyosin structure and dynamics[44]. We observed that the activity of RhoA at the
268 apical side was significantly decreased in crowded cells, while the activity of Rac1 was significantly
269 increased (Fig. 4c, d). Given that RhoA promotes the assembly of stress fibers[45] and Rac1 mediates
270 branched actin polymerization[46], these results suggest that prolonged crowding affects membrane
271 tension and cytoskeleton assembly.

272 To evaluate whether the organization of cortical actin was regulated by prolonged crowding, we
273 performed 3D confocal imaging of cortical actin. We found that the height of apical F-actin was
274 significantly increased in crowded cells compared to uncrowded cells (Fig. 4e, f and Fig. S7c, d).
275 Furthermore, the orientation of actin fibers was altered by prolonged crowding, with fibers in
276 crowded cells exhibiting a more vertical orientation (> 70°related to the base plane), whereas fibers
277 in uncrowded cells were primarily parallel (< 20°) (Fig. 4g). These results suggest that prolonged
278 crowding triggers the remodeling of both plasma membrane and cortical actin.

279 Previous studies have indicated that membrane-to-cortex attachment (MCA) and cell protrusions
280 (such as blebs) are regulated by the Laplace pressure, the pressure difference across plasma
281 membranes[47]. As a key regulator of cell shape and volume, Laplace pressure influences various
282 cellular processes, including cell migration, proliferation, necrosis, apoptosis, material transportation,
283 and signal transduction[47]. To investigate the biophysical mechanism underlying the nSCTT of plasma
284 membranes induced by prolonged crowding, we analyzed Laplace pressure in cells exposed to
285 different crowding strains using a previously reported micro pressure system[48]. We found that
286 Laplace pressure in crowded cells was significantly higher than in uncrowded cells (Fig. 4h and i).

287 To further explore the potential impacts of Laplace pressure and membrane tension on the
288 nanoscale topography of plasma membranes, we performed Monte Carlo (MC) simulations of a
289 membrane-cortical actin system (Fig. 4j and Fig. S8). In this MC model, plasma membranes are
290 represented as a fluctuating elastic surface, while cortical actin is modeled as a uniform square mesh

framework. The plasma membranes are discretized into square lattices, with each lattice capable of accommodating a transmembrane protein. These transmembrane proteins (linker proteins) connect the plasma membranes to the cortical actin via a harmonic potential[49,50]. The resulting snapshots, as shown in Fig. 4k, clearly demonstrate that increased Laplace pressure $\Delta\overline{p}$ and decreased membrane tension $\overline{\tau}$ contribute to pronounced bulges and large deformations of the plasma membrane. To quantify these observations, we analyzed the relative roughness $\xi_{\perp}$ of the cell membrane as a function of both Laplace pressure and membrane tension. The rescaled roughness $\overline{\xi}_{\perp}$ increased with higher Laplace pressure and lower membrane tension (Fig. 4l). These modeling results, in conjunction with our cellular crowding experiments, provide compelling evidence that the nanoscale topography of plasma membranes is precisely regulated by the interplay between Laplace pressure and membrane tension.

In our MC model, we observed that the detachment of membrane from the cortical actin is regulated in response to changes in Laplace pressure $\Delta\overline{p}$ and membrane tension $\overline{\tau}$. Specifically, at a fixed value of $\overline{\tau}$, when the applied $\Delta\overline{p}$ exceeds a critical threshold, the proportion ϕ of linker proteins bound to the cortical actin abruptly drops to zero, indicating complete detachment of the cell membrane from the cortical actin. A similar behavior is observed when $\overline{\tau}$ is reduced to a critical value at fixed $\Delta\overline{p}$ (Fig. 4m). Additionally, increasing the density of linker proteins (C_p) significantly reduces membrane roughness under constant $\Delta\overline{p}$ and $\overline{\tau}$ (Fig. 4n), underscoring the essential role of MCA in the regulation of the nanoscale topography of plasma membranes through the interplay of Laplace pressure and membrane tension. In summary, these findings suggest that the nSCTT of plasma membranes arises from the membrane-to-cortex detachment, driven by an increase in Laplace pressure and a decrease in membrane tension. This mechanism highlights the critical influence of mechanical forces and molecular interactions in shaping membrane morphology.

To further explore the regulation of membrane domain aggregation by Laplace pressure and membrane tension, we incorporated membrane domains into our computational model. These domains exhibit short-range attractive interactions and undergo dynamic fission and merging processes. The distribution of membrane domains is significantly influenced by changes in Laplace

318 pressure $\Delta\overline{p}$ and membrane tension $\overline{\tau}$. At small $\Delta\overline{p}$, membrane domains tend to coalesce into a
319 single large domain. However, as Laplace pressure increases, this single domain separates into
320 multiple smaller domains (Fig. 4o). To quantitatively analyze the spatial distribution of membrane
321 domains, we calculated the pair distribution function *g*(r), where a higher *g*(r) value indicates a
322 greater probability of finding two membrane domains at a distance r. As shown in Fig. 4p, an
323 increase in $\Delta\overline{p}$ results in a larger initial spike in g (r) (where (g(r)>1), suggesting that elevated
324 Laplace pressure reduces the propensity for membrane domain aggregation. Conversely, an increase
325 in membrane tension also leads to a larger initial spike of g(r), indicating that higher membrane
326 tension promotes the aggregation of membrane domains (Fig. 4p). Next, we explored the influence
327 of linker proteins on membrane domain aggregation within our MC simulations. Our analysis
328 indicated that augmenting the density of linker protein C_p enhances the aggregation of membrane
329 domains (Fig. 4q). These results underscore that the aggregation of membrane domains is disrupted
330 by increased Laplace pressure and membrane tension under conditions of prolonged crowding.

331 To elucidate the mechanism governing the regulation of lipid membrane domain aggregation by
332 Laplace pressure and membrane tension, we estimated the bending energy of the multicomponent
333 membrane using a discretized Helfrich Hamiltonian[51]. At low raft-raft contact energy U, the
334 membrane domains are uniformly distributed across the cell membrane. As U increases, these
335 domains tend to coalesce into a single, larger domain. The change in bending energy ΔE_b rises
336 with the increasing raft-raft contact energy U, suggesting that the aggregation of membrane
337 domains is energetically unfavorable (Fig. 4r). This analysis of bending energy reveals that both
338 elevated Laplace pressure and reduced membrane tension increase the energy change ΔE_b, thereby
339 raising the energetic cost for membrane domain aggregation.

340 To further investigate the effects of membrane curvature on the aggregation of membrane domains,
341 we conducted μs-scale coarse-grained (CG) molecular dynamics (MD) simulations of
342 three-component vesicles (DPPC: 50%; DUPC: 30%; CHOL: 20%) with two different radii (10 nm
343 and 20 nm) using the Martini CG model[52,53]. As illustrated in the system snapshots and normalized
344 lateral contacts of DUPC lipids (Fig. 4s and t), DPPC/DUPC/CHOL vesicles underwent pronounced
345 aggregation of membrane domains in both vesicle sizes. However, the larger vesicles (r = 20 nm),

346 characterized by reduced membrane curvature, displayed significantly enhanced aggregation of
347 membrane domains. These results suggest that the local nanoscale topography with higher membrane
348 curvature inhibits the aggregation of membrane domains. Collectively, these findings highlight that
349 the aggregation of membrane domains is disrupted under prolonged crowding condition through a
350 complex interplay of mechanical forces and molecular interactions.
351
352

353 **Suppressing the pressure-sensation of membrane domains inhibits tumor invasion**

354 To empirically validate the predictions from our simulations, we investigated the distribution of
355 ERM proteins (ezrin, radixin, and moesin), which are known to mediate MCA by linking plasma
356 membranes to cortical actin[54,55], in the cellular crowding model. Immunofluorescence staining with
357 an antibody specific to phosphorylated ERM (pERM), the active membrane- and actin-bound form
358 of ERM, revealed a progressive reduction in pERM levels at the apical membrane as crowding strain
359 increased (Fig. 5a and b). Furthermore, this reduction in apical pERM levels in crowded cells
360 persisted for 3 days after transitioning to sparse culture conditions (Fig. 5c and d). These findings
361 demonstrate that prolonged crowding leads to a sustained decrease in activated ERM levels,
362 indicating a form of mechanomemory in cancer cells.
363 Our simulation results revealed that enhanced MCA confers resistance against the nSCTT of
364 plasma membranes and prevents the disaggregation of membrane domains under prolonged
365 crowding conditions (Fig. 4n and q). To experimentally validate this prediction, we employed a
366 Lyn-FRB and $Ezrin_{abd}$-FKBP activation system[42], which incorporates a constitutively active F-actin
367 binding domain of Ezrin ($Ezrin_{abd}$T567D). Following rapamycin treatment, $Ezrin_{abd}$T567D was
368 efficiently recruited to the membrane, leading to a significant increase in cortical actin density (Fig.
369 5e, and Fig. S9a-c). Acute reinforcement of MCA through recruitment of FKBP-$Ezrin_{abd}$T567D to
370 plasma membranes resulted in a marked reduction in both membrane protrusions and apical F-actin
371 height in crowded cells (Fig. 5f-g, and Fig. S9d-e). Furthermore, enhanced MCA via
372 FKBP-$Ezrin_{abd}$T567D activation significantly increased the aggregation of membrane domains, as
373 evidenced by both fluorescence intensity and the number of CTxB clusters in crowded cells treated
374 with rapamycin compared to untreated cells (Fig. 5h-k). These results demonstrate that the

375 aggregation of membrane domains, disrupted by prolonged crowding, can be rescued by inhibiting
376 the nSCTT of plasma membranes through the enhancement of MCA.

377 Next, we investigated whether experimentally enhancing MCA could suppress the invasion driven
378 by prolonged crowding in the cellular crowding model. Transwell invasion assays revealed that
379 enhancing MCA through FKBP-Ezrin$_{abd}$T567D activation significantly inhibited the invasion of
380 cancer cells exposed to prolonged crowding (Fig. 5l and m). Immunofluorescence staining of
381 cortactin at the basal membrane demonstrated that the number of invadopodia per cell in crowded
382 cells was markedly reduced by FKBP-Ezrin$_{abd}$T567D activation compared to control cells (Fig. 5n-p).
383 Furthermore, FKBP-Ezrin$_{abd}$T567D activation also suppressed ECM degradation, as evidenced by
384 experiments using Cy5-conjugated gelatin hydrogels (Fig. 5q-s). These results suggest that
385 enhancing membrane domain aggregation by strengthening MCA efficiently rescues the prolonged
386 crowding-driven invasiveness.

387 To evaluate whether enhancing MCA could suppress tumor invasion *in vivo,* we established a
388 subcutaneous mouse xenograft model using FKBP-mCherry$^+$ or FKBP-Ezrin$_{abd}$T567D-mCherry$^+$
389 HeLa cells. At one-week post-cancer cell inoculation, the mice were treated with rapamycin (Fig. 6a).
390 Consistent with the *in vitro* data (Fig. S9a), F-actin was recruited to the cell membrane in
391 FKBP-Ezrin$_{abd}$T567D-mCherry$^+$ xenografts after two weeks of rapamycin administration, contrasting
392 with FKBP-mCherry$^+$ xenografts (Fig. 6b). Immunofluorescence analysis using anti-sodium
393 potassium ATPase (Na^+/K^+ ATPase) antibody for membrane labeling revealed a significant reduction
394 in the fractal dimension of plasma membranes in crowded cells of FKBP-Ezrin$_{abd}$T567D-mCherry$^+$
395 xenografts compared to FKBP-mCherry$^+$ xenografts (Fig. 6c). Furthermore, elevated levels of
396 membrane domain markers (Caveolin-1 and Flotillin-1) were detected in
397 FKBP-Ezrin$_{abd}$T567D-mCherry$^+$ cells compared to FKBP-mCherry$^+$ cells (Fig. 6d-g). These findings
398 demonstrate that enhanced MCA effectively suppresses the nSCTT of plasma membranes and
399 mitigates membrane domain disaggregation in crowded cancer cells within xenografts.

400 Next, we investigated the invasive growth patterns in xenografts with or without strengthening
401 MCA. Hematoxylin and eosin (H&E) staining demonstrated that FKBP-mCherry$^+$ xenografts
402 exhibited deeper invasion into the muscle layer (Fig. 6h and i). In contrast,
403 FKBP-Ezrin$_{abd}$T567D-mCherry$^+$ xenografts displayed well-defined pushing tumor borders,
404 effectively segregating cancer cells from the adjacent muscle layer with only minor focal invasions

405 (Fig. 6h). Immunofluorescence staining for RAB5A further reveled that the invasive edge of tumors
406 in FKBP-Ezrin$_{abd}$T567D-mCherry^{+} xenografts exhibited reduced invasiveness compared to
407 FKBP-mCherry^{+} xenografts (Fig. 6j and k). Additionally, the inhibitory effect of MCA enhancement
408 on tumor invasion was confirmed by comparing FKBP-Ezrin$_{abd}$T567D-mCherry^{+} HeLa cell
409 xenografts with and without rapamycin treatment (Fig. S10). Taken together, these results
410 demonstrate that preventing membrane domain disaggregation through MCA enhancement
411 effectively suppresses cancer cell invasiveness *in vivo*.

412 **DISCUSSION**

413 Growing in confined spaces, cancer cells push and stretch solid components of the surrounding tissue
414 and thus experience situations of crowding[8]. Recent studies have shown that crowding triggers cell
415 extrusion and induces cell migration during embryonic development and tumor progression[56-59]. Here,
416 using a spontaneous crowding model composed of a freely growing monoclonal cell sheet, we found
417 that prolonged crowding drives cancer cell invasiveness with memory retention by triggering a
418 nanoscale topography transition of plasma membranes from a smooth to a corrugated state.
419 Combining mechanical modeling, genetic manipulations, and biophysical measurements, we further
420 found that the prolonged crowding-triggered nSCTT of plasma membranes disrupts the aggregation
421 of membrane domains to drive tumor invasion (Fig. 6l).

422 Plasma membranes of cancer cells exhibit complex and irregular shapes. Analyses using fractal
423 geometry are already used to efficiently estimate the geometrical shapes observed during tumor
424 progression and for ascertaining correlations with pathological processes[60]. For example, skin cancer
425 can be modeled by calculating fractals to evaluate the invasiveness of cancer cells[60]. The fractal
426 dimension of AFM maps is analyzed for three stages of progression towards cervical cancer, from
427 normal through immortal to malignant cells[61]. Here, we identified that prolonged crowding increases
428 the Laplace pressure and decreases membrane tension, which induces nanoscale protrusions at the
429 apical plasma membrane of cancer cells. The aggregation of membrane domains suppressed by the
430 nSCTT of plasma membranes disrupts epithelial integrity and drives cancer cell invasiveness.

431 Although controversies about the composition, properties, and even the existence of membrane
432 domains remain unresolved[62], previous studies have demonstrated that most transmembrane proteins
433 are found in membrane domains to serve as signaling platforms or connect cortical actin for
434 controlling cell behaviors[63]. Recent observations of model membranes reported that macroscopic
435 membrane domains exist in membrane regions with nanoscale smooth topography[39]. Another study
436 has shown that pharmacological disruption of rafts using MβCD decreases CD44 retention inside
437 membrane domains and promotes CD44 interaction with ezrin to drive cell migration[64]. In addition,
438 oncogenic mutants of RAS proteins (encoded by *HRAS, KRAS, NRAS*) are localized to the inner
439 leaflet of the plasma membranes, and the assembly of RAS nanoscale clusters is known to depend on
440 the interactions between plasma membrane lipids and RAS molecules[65,66]. In light of our findings,

441 RAS activation may be driven by the aggregation of membrane domains in cells experiencing the
442 nSCTT of plasma membranes triggered by prolonged crowding.

443 As a transmembrane pressure of cells, the Laplace pressure which is the difference between
444 intracellular and extracellular pressures can rapidly reprogram cell shape and regulate cell
445 migration[47,67]. Membrane tension, which arises from the combined contributions of osmotic pressure,
446 in-plane tension, and cytoskeletal forces, remodel membrane topology and influence cellular
447 function[40]. In tumor environments, the mechanical characteristics of crowding lead to changes in
448 both the Laplace pressure and membrane tension of cancer cells. These cells' behavior regulation in
449 crowded environments maybe mediated by mechanosensitive ion transporters and channels affected
450 by Laplace pressure and membrane tension[68,69]. Our findings demonstrate that the nanoscale
451 smooth-corrugated topography transition of plasma membranes induced by crowding can
452 significantly enhance cancer cell invasiveness.

453 Our experiments demonstrated that plasma membranes exhibit a configuration of nanoscale
454 topography that is consistent with cortical actin protrusion. Recent studies have reported that tumor
455 cells migrate through crowded environments via large bleb protrusion controlled by actin filament at
456 the cell front to break apart ECM[70,71]. ERM proteins, which tether the membrane to cortical actin of
457 cells, restrict local membrane protrusions and inhibit cancer cell migration[42]. This is consistent with
458 our experimental findings showing that enhancing membrane-to-cortex attachment by
459 FKBP-Ezrin$_{abd}$T567D significantly inhibits the prolonged crowding-induced nSCTT of plasma
460 membranes and the invasiveness of cancer cells.

461 The geometrical irregularity of tumor boundaries has been implicated in the development and
462 progression of cancers such as skin, breast, and lung cancer[60,72,73]. The application of fractal
463 geometry for analyzing the surface of human cervical and breast cancer cells has shown considerable
464 promise for estimating cancer stages[61,74,75]. Abnormal changes in the shape of the plasma membranes,
465 including bending and protrusion, promote the migration and invasion of cancer cells[54]. Our
466 experiments and modeling results demonstrate that prolonged crowding drives cancer cell
467 invasiveness by triggering a nSCTT of plasma membranes. Inhibiting the nSCTT by enhancing MCA
468 effectively suppresses cancer cell invasiveness induced by prolonged crowding. Our findings provide
469 clues for potential clinical strategies targeting the nanoscale topography of plasma membranes for
470 preventing carcinoma invasion. In particular, given the essential roles of ERM proteins in regulating

471 crowding-driven invasiveness, it will be interesting to further explore if certain small molecules or
472 gene-targeting entities could be identified to suppress ERM dephosphorylation and thus reinforce
473 MCA when delivered to the tumor tissues. These new agents may hinder the progression of tumors
474 toward a more malignant stage by normalizing the plasma membrane topography of cancer cells
475 subjected to prolonged crowding.
476

477 **REFERENCES**

478 1 Hayward, M.-K., Muncie, J. M. & Weaver, V. M. Tissue mechanics in stem cell fate, development, and cancer.
479 *Dev Cell* **56**, 1833-1847 (2021). https://doi.org:10.1016/j.devcel.2021.05.011
480 2 Yuan, S., Almagro, J. & Fuchs, E. Beyond genetics: driving cancer with the tumour microenvironment behind the
481 wheel. *Nat Rev Cancer* **24**, 274-286 (2024). https://doi.org:10.1038/s41568-023-00660-9
482 3 Eisenhoffer, G. T. *et al.* Crowding induces live cell extrusion to maintain homeostatic cell numbers in epithelia.
483 *Nature* **484**, 546-549 (2012). https://doi.org:10.1038/nature10999
484 4 Nia, H. T., Munn, L. L. & Jain, R. K. Physical traits of cancer. *Science* **370** (2020).
485 https://doi.org:10.1126/science.aaz0868
486 5 Wirtz, D., Konstantopoulos, K. & Searson, P. C. The physics of cancer: the role of physical interactions and
487 mechanical forces in metastasis. *Nat Rev Cancer* **11**, 512-522 (2011). https://doi.org:10.1038/nrc3080
488 6 van Helvert, S., Storm, C. & Friedl, P. Mechanoreciprocity in cell migration. *Nat Cell Biol* **20**, 8-20 (2018).
489 https://doi.org:10.1038/s41556-017-0012-0
490 7 Tse, J. M. *et al.* Mechanical compression drives cancer cells toward invasive phenotype. *Proc Natl Acad Sci USA*
491 **109**, 911-916 (2012). https://doi.org:10.1073/pnas.1118910109
492 8 Jain, R. K., Martin, J. D. & Stylianopoulos, T. The role of mechanical forces in tumor growth and therapy. *Annu*
493 *Rev Biomed Eng* **16**, 321-346 (2014). https://doi.org:10.1146/annurev-bioeng-071813-105259
494 9 Fiore, V. F. *et al.* Mechanics of a multilayer epithelium instruct tumour architecture and function. *Nature* **585**,
495 433-439 (2020). https://doi.org:10.1038/s41586-020-2695-9
496 10 Bansaccal, N. *et al.* The extracellular matrix dictates regional competence for tumour initiation. *Nature* **623**,
497 828-835 (2023). https://doi.org:10.1038/s41586-023-06740-y
498 11 Liu, Y. J. *et al.* Confinement and low adhesion induce fast amoeboid migration of slow mesenchymal cells. *Cell*
499 **160**, 659-672 (2015). https://doi.org:10.1016/j.cell.2015.01.007
500 12 Ruprecht, V. *et al.* Cortical contractility triggers a stochastic switch to fast amoeboid cell motility. *Cell* **160**,
501 673-685 (2015). https://doi.org:10.1016/j.cell.2015.01.008
502 13 Lomakin, A. J. *et al.* The nucleus acts as a ruler tailoring cell responses to spatial constraints. *Science* **370** (2020).
503 https://doi.org:10.1126/science.aba2894
504 14 Venturini, V. *et al.* The nucleus measures shape changes for cellular proprioception to control dynamic cell
505 behavior. *Science* **370** (2020). https://doi.org:10.1126/science.aba2644
506 15 Nader, G. P. F. *et al.* Compromised nuclear envelope integrity drives TREX1-dependent DNA damage and tumor
507 cell invasion. *Cell* **184**, 5230-5246 e5222 (2021). https://doi.org:10.1016/j.cell.2021.08.035
508 16 Le Berre, M., Zlotek-Zlotkiewicz, E., Bonazzi, D., Lautenschlaeger, F. & Piel, M. Methods for two-dimensional cell
509 confinement. *Methods Cell Biol* **121**, 213-229 (2014). https://doi.org:10.1016/b978-0-12-800281-0.00014-2
510 17 Cambria, E. *et al.* Linking cell mechanical memory and cancer metastasis. *Nat Rev Cancer* (2024).
511 https://doi.org:10.1038/s41568-023-00656-5
512 18 Watson, A. W. *et al.* Breast tumor stiffness instructs bone metastasis via maintenance of mechanical
513 conditioning. *Cell Rep* **35** (2021). https://doi.org:10.1016/j.celrep.2021.109293
514 19 Cambria, E. *et al.* Linking cell mechanical memory and cancer metastasis. *Nature Reviews Cancer* **24**, 216-228
515 (2024). https://doi.org:10.1038/s41568-023-00656-5
516 20 Yang, S. *et al.* ETV4 is a mechanical transducer linking cell crowding dynamics to lineage specification. *Nat Cell*
517 *Biol* **26**, 903-916 (2024). https://doi.org:10.1038/s41556-024-01415-w
518 21 Messal, H. A. *et al.* Tissue curvature and apicobasal mechanical tension imbalance instruct cancer
519 morphogenesis. *Nature* **566**, 126-130 (2019). https://doi.org:10.1038/s41586-019-0891-2
520 22 Eckert, M. A. *et al.* Twist1-induced invadopodia formation promotes tumor metastasis. *Cancer Cell* **19**, 372-386

521 (2011). https://doi.org:10.1016/j.ccr.2011.01.036
522 23 Murphy, D. A. & Courtneidge, S. A. The 'ins' and 'outs' of podosomes and invadopodia: characteristics,
523 formation and function. *Nat Rev Mol Cell Biol* **12**, 413-426 (2011). https://doi.org:10.1038/nrm3141
524 24 Eddy, R. J., Weidmann, M. D., Sharma, V. P. & Condeelis, J. S. Tumor Cell Invadopodia: Invasive Protrusions that
525 Orchestrate Metastasis. *Trends Cell Biol* **27**, 595-607 (2017). https://doi.org:10.1016/j.tcb.2017.03.003
526 25 Li, C. X. *et al.* MicroRNA-21 preserves the fibrotic mechanical memory of mesenchymal stem cells. *Nat Mater*
527 **16**, 379-389 (2017). https://doi.org:10.1038/nmat4780
528 26 Yang, C., Tibbitt, M. W., Basta, L. & Anseth, K. S. Mechanical memory and dosing influence stem cell fate. *Nat*
529 *Mater* **13**, 645-652 (2014). https://doi.org:10.1038/nmat3889
530 27 Lambrecht, B. N., Vanderkerken, M. & Hammad, H. The emerging role of ADAM metalloproteinases in
531 immunity. *Nat Rev Immunol* **18**, 745-758 (2018). https://doi.org:10.1038/s41577-018-0068-5
532 28 Sezgin, E., Levental, I., Mayor, S. & Eggeling, C. The mystery of membrane organization: composition, regulation
533 and roles of lipid rafts. *Nat Rev Mol Cell Biol* **18**, 361-374 (2017). https://doi.org:10.1038/nrm.2017.16
534 29 Lingwood, D. & Simons, K. Lipid rafts as a membrane-organizing principle. *Science* **327**, 46-50 (2010).
535 https://doi.org:10.1126/science.1174621
536 30 Martinez-Outschoorn, U. E., Sotgia, F. & Lisanti, M. P. Caveolae and signalling in cancer. *Nat Rev Cancer* **15**,
537 225-237 (2015). https://doi.org:10.1038/nrc3915
538 31 Kabbani, A. M., Raghunathan, K., Lencer, W. I., Kenworthy, A. K. & Kelly, C. V. Structured clustering of the
539 glycosphingolipid GM1 is required for membrane curvature induced by cholera toxin. *Proc Natl Acad Sci USA*
540 **117**, 14978-14986 (2020). https://doi.org:10.1073/pnas.2001119117
541 32 Cheng, M. *et al.* MβCD inhibits SFTSV entry by disrupting lipid raft structure of the host cells. *Antivir Res* **231**,
542 106004 (2024).
543 33 Dongre, A. & Weinberg, R. A. New insights into the mechanisms of epithelial-mesenchymal transition and
544 implications for cancer. *Nat Rev Mol Cell Biol* **20**, 69-84 (2019). https://doi.org:10.1038/s41580-018-0080-4
545 34 Shigetomi, K., Ono, Y., Matsuzawa, K. & Ikenouchi, J. Cholesterol-rich domain formation mediated by ZO
546 proteins is essential for tight junction formation. *Proc Natl Acad Sci USA* **120**, e2217561120 (2023).
547 https://doi.org:10.1073/pnas.2217561120
548 35 Otani, T. & Furuse, M. Tight junction structure and function revisited. *Trends Cell Biol* **30**, 805-817 (2020).
549 https://doi.org:10.1016/j.tcb.2020.08.004
550 36 Rambur, A. *et al.* Sequential Ras/MAPK and PI3K/AKT/mTOR pathways recruitment drives basal extrusion in the
551 prostate-like gland of Drosophila. *Nature Communications* **11**, 2300 (2020).
552 https://doi.org:10.1038/s41467-020-16123-w
553 37 Castellino, R. C. & Durden, D. L. Mechanisms of Disease: the PI3K–Akt–PTEN signaling node—an intercept point
554 for the control of angiogenesis in brain tumors. *Nature Clinical Practice Neurology* **3**, 682-693 (2007).
555 https://doi.org:10.1038/ncpneuro0661
556 38 Fruman, D. A. & Rommel, C. PI3K and cancer: lessons, challenges and opportunities. *Nature Reviews Drug*
557 *Discovery* **13**, 140-156 (2014). https://doi.org:10.1038/nrd4204
558 39 Yoon, T. Y. *et al.* Topographic control of lipid-raft reconstitution in model membranes. *Nat Mater* **5**, 281-285
559 (2006). https://doi.org:10.1038/nmat1618
560 40 Lipowsky, R. Remodeling of membrane shape and topology by curvature elasticity and membrane tension. *Adv*
561 *Bio* **6** (2021). https://doi.org:10.1002/adbi.202101020
562 41 Colom, A. *et al.* A fluorescent membrane tension probe. *Nat Chem* **10**, 1118-1125 (2018).
563 https://doi.org:10.1038/s41557-018-0127-3
564 42 Bisaria, A., Hayer, A., Garbett, D., Cohen, D. & Meyer, T. Membrane proximal F-actin restricts local membrane

565 protrusions and directs cell migration. *Science* **368**, 1205-1210 (2020). https://doi.org:10.1126/science.aay7794
566 43 Fritz, R. D. *et al.* SrGAP2-dependent integration of membrane geometry and Slit-Robo-repulsive cues regulates
567 fibroblast contact inhibition of locomotion. *Dev Cell* **35**, 78-92 (2015).
568 https://doi.org:10.1016/j.devcel.2015.09.002
569 44 Murali, A. & Rajalingam, K. Small Rho GTPases in the control of cell shape and mobility. *Cell Mol Life Sci* **71**,
570 1703-1721 (2014). https://doi.org:10.1007/s00018-013-1519-6
571 45 Burridge, K. & Guilluy, C. Focal adhesions, stress fibers and mechanical tension. *Exp Cell Res* **343**, 14-20 (2016).
572 https://doi.org:https://doi.org/10.1016/j.yexcr.2015.10.029
573 46 Sathe, M. *et al.* Small GTPases and BAR domain proteins regulate branched actin polymerisation for clathrin
574 and dynamin-independent endocytosis.
575 47 Wang, X. *et al.* Effects of the Laplace pressure on the cells during cytokinesis. *iScience* **24**, 102945 (2021).
576 https://doi.org:10.1016/j.isci.2021.102945
577 48 Petrie, R. J. & Koo, H. Direct measurement of intracellular pressure. *Current Protoc Cell Bio* **63** (2014).
578 https://doi.org:10.1002/0471143030.cb1209s63
579 49 Li, L. *et al.* Control of cell membrane receptor condensation by adhesion to supported bilayers with nanoscale
580 topography. *Commun Phys* **7**, 174 (2024). https://doi.org:10.1038/s42005-024-01670-1
581 50 Li, L., Hu, J., Różycki, B. & Song, F. Intercellular receptor–ligand binding and thermal fluctuations facilitate
582 receptor aggregation in adhering membranes. *Nano Lett* **20**, 722-728 (2020).
583 https://doi.org:10.1021/acs.nanolett.9b04596
584 51 Costa, M. N., Radhakrishnan, K. & Edwards, J. S. Monte Carlo simulations of plasma membrane corral-induced
585 EGFR clustering. *J Biotechnol* **151**, 261-270 (2011). https://doi.org:10.1016/j.jbiotec.2010.12.009
586 52 Marrink, S. J., Risselada, H. J., Yefimov, S., Tieleman, D. P. & de Vries, A. H. The MARTINI force field: coarse
587 grained model for biomolecular simulations. *J Phys Chem B* **111**, 7812-7824 (2007).
588 https://doi.org:10.1021/jp071097f
589 53 Qi, Y. *et al.* CHARMM-GUI Martini maker for coarse-grained simulations with the Martini force field. *J Chem*
590 *Theory Comput* **11**, 4486-4494 (2015). https://doi.org:10.1021/acs.jctc.5b00513
591 54 Tsujita, K. *et al.* Homeostatic membrane tension constrains cancer cell dissemination by counteracting BAR
592 protein assembly. *Nat Commun* **12**, 5930 (2021). https://doi.org:10.1038/s41467-021-26156-4
593 55 Conti, S. *et al.* Membrane to cortex attachment determines different mechanical phenotypes in LGR5+ and
594 LGR5- colorectal cancer cells. *Nat Commun* **15**, 3363 (2024). https://doi.org:10.1038/s41467-024-47227-2
595 56 Eisenhoffer, G. T. & Rosenblatt, J. Bringing balance by force: live cell extrusion controls epithelial cell numbers.
596 *Trends Cell Biol* **23**, 185-192 (2013). https://doi.org:10.1016/j.tcb.2012.11.006
597 57 Marinari, E. *et al.* Live-cell delamination counterbalances epithelial growth to limit tissue overcrowding. *Nature*
598 **484**, 542-545 (2012). https://doi.org:10.1038/nature10984
599 58 Fadul, J. *et al.* KRas-transformed epithelia cells invade and partially dedifferentiate by basal cell extrusion. *Nat*
600 *Commun* **12**, 7180 (2021). https://doi.org:10.1038/s41467-021-27513-z
601 59 Chang, T. T., Thakar, D. & Weaver, V. M. Force-dependent breaching of the basement membrane. *Matrix Biol*
602 **57-58**, 178-189 (2017). https://doi.org:10.1016/j.matbio.2016.12.005
603 60 Hussain, R. J., Deviha, V.S., Rengarajan, P. . Analysing the invasiveness of skin cancer using fractals. *IJERA* **2**, 8
604 (2012).
605 61 Guz, N. V., Dokukin, M. E., Woodworth, C. D., Cardin, A. & Sokolov, I. Towards early detection of cervical cancer:
606 Fractal dimension of AFM images of human cervical epithelial cells at different stages of progression to cancer.
607 *Nanomedicine* **11**, 1667-1675 (2015). https://doi.org:10.1016/j.nano.2015.04.012
608 62 Levental, I., Levental, K. R. & Heberle, F. A. Lipid rafts: controversies resolved, mysteries remain. *Trends Cell Biol*

609 **30**, 341-353 (2020). https://doi.org:10.1016/j.tcb.2020.01.009
610 63 Viola, A. & Gupta, N. Tether and trap: regulation of membrane-raft dynamics by actin-binding proteins. *Nat Rev*
611 *Immunol* **7**, 889-896 (2007). https://doi.org:10.1038/nri2193
612 64 Donatello, S. *et al.* Lipid raft association restricts CD44-ezrin interaction and promotion of breast cancer cell
613 migration. *Am J Pathol* **181**, 2172-2187 (2012). https://doi.org:10.1016/j.ajpath.2012.08.025
614 65 Simanshu, D. K., Philips, M. R. & Hancock, J. F. Consensus on the RAS dimerization hypothesis: Strong evidence
615 for lipid-mediated clustering but not for G-domain-mediated interactions. *Mol Cell* **83**, 1210-1215 (2023).
616 https://doi.org:10.1016/j.molcel.2023.03.008
617 66 Zhou, Y. & Hancock, J. F. RAS nanoclusters are cell surface transducers that convert extracellular stimuli to
618 intracellular signalling. *FEBS Lett* **597**, 892-908 (2023). https://doi.org:10.1002/1873-3468.14569
619 67 Chengappa, P., Sao, K., Jones, T. M. & Petrie, R. J. Intracellular Pressure: A Driver of Cell Morphology and
620 Movement. *Int Rev Cell Mol Biol* **337**, 27 (2018).
621 68 Kuromiya, K. *et al.* Calcium sparks enhance the tissue fluidity within epithelial layers and promote apical
622 extrusion of transformed cells. *Cell Rep* **40**, 111078 (2022). https://doi.org:10.1016/j.celrep.2022.111078
623 69 Lewis, A. H. & Grandl, J. Mechanical sensitivity of Piezo1 ion channels can be tuned by cellular membrane
624 tension. *eLife* **4**, e12088 (2015). https://doi.org:10.7554/eLife.12088
625 70 Garcia-Arcos, J. M., Jha, A., Waterman, C. M. & Piel, M. Blebology: principles of bleb-based migration. *Trends*
626 *Cell Biol* **34**, 838-853 (2024). https://doi.org:10.1016/j.tcb.2024.02.009
627 71 Driscoll, M. K. *et al.* Proteolysis-free amoeboid migration of melanoma cells through crowded environments via
628 bleb-driven worrying. *Dev Cell* **59**, 2414-2428.e2418 (2024). https://doi.org:10.1016/j.devcel.2024.05.024
629 72 Machireddy, A. *et al.* Early prediction of breast cancer therapy response using multiresolution fractal analysis of
630 DCE-MRI parametric maps. *Tomography* **5**, 90-98 (2019). https://doi.org:10.18383/j.tom.2018.00046
631 73 Lennon, F. E. *et al.* Lung cancer-a fractal viewpoint. *Nat Rev Clin Oncol* **12**, 664-675 (2015).
632 https://doi.org:10.1038/nrclinonc.2015.108
633 74 Dokukin, M. E., Guz, N. V., Woodworth, C. D. & Sokolov, I. Emergence of fractal geometry on the surface of
634 human cervical epithelial cells during progression towards cancer. *New Journal of Physics* **17** (2015).
635 https://doi.org:10.1088/1367-2630/17/3/033019
636 75 Krasowska, M., Grzywna, Z. J., Mycielska, M. E. & Djamgoz, M. B. A. Fractal analysis and ionic dependence of
637 endocytotic membrane activity of human breast cancer cells. *Eur Biophys J* **38**, 1115-1125 (2009).
638 https://doi.org:10.1007/s00249-009-0516-z
639 76 Abraham, M. J. *et al.* GROMACS: High performance molecular simulations through multi-level parallelism from
640 laptops to supercomputers. *SoftwareX* **1-2**, 19-25 (2015). https://doi.org:10.1016/j.softx.2015.06.001
641 77 Risselada, H. J. & Marrink, S. J. The molecular face of lipid rafts in model membranes. *Proc Natl Acad Sci USA*
642 **105**, 17367-17372 (2008). https://doi.org:10.1073/pnas.0807527105
643 78 Humphrey, W., Dalke, A. & Schulten, K. VMD: Visual molecular dynamics. *J Mol Graph Model* **14**, 33-38 (1996).
644 https://doi.org:10.1016/0263-7855(96)00018-5
645 79 Hassan, R., Garzon, M. A., Gao, W. & Ahmadpoor, F. Entropic pressure on fluctuating solid membranes. *J Mech*
646 *Phys Solids* **183**, 105523 (2024). https://doi.org:10.1016/j.jmps.2023.105523

647
648

649 **METHODS**

650 **Mouse lines**

651 SPF male BALB/c nude mice aged 3-4 weeks and weighing 16-18 g were purchased from Vital
652 River Laboratory Animal Technology Co., Ltd. Mice were bred and reared in the animal facility of
653 Tsinghua University at 22 °C with a 12-hour light/dark cycle (lighting time 7:00-19:00). Food and
654 water are freely available. All animal studies were conducted under the guidance of the Animal Care
655 and Utilization Committee (IACUC) of Tsinghua University. According to the National Institutes of
656 Health "Animal Ethical Use Guidelines", the experimental procedure has been approved by the
657 Laboratory Animal Care and Use Management Committee of Tsinghua University and the Beijing
658 Municipal Science and Technology Commission (SYXK-2019-0044).

659 **Human tissues**

660 Samples of human breast cancer, skin cancer, and cervical cancer (paraffin sections) were obtained
661 from patients who had undergone surgery at the Dezhou Second People's Hospital. The cases were
662 classified according to the World Health Organization classification criteria of the tumors. The
663 samples were collected with patient consent, following approval by the Institutional Committee for
664 the Welfare of Human Subjects.

665 **Maintenance of cell lines**

666 HeLa, A431, and MC38 cells were cultured in Dulbecco's modified eagle medium (DMEM) medium
667 (containing 4.5 g/L glucose, L-glutamine and sodium pyruvate) supplemented with 10% fetal bovine
668 serum (FBS; Life technologies, CA, USA), and 100 IU/mg penicillin-streptomycin (Life
669 technologies, CA, USA), and 1% (v/v) non-essential amino acids (NEAA; Life technologies, CA,
670 USA).

671 **Plasmid construction and transfection**

672 Cells were transiently transfected with plasmid DNA (pEF1-Lifeact-mCherry, pEYFP-membrane,
673 pTriEx4-Rac1-2G and pTriEx-RhoA-2G) using Lipofectamine 2000 (PN: 11668030, Invitrogen),
674 according to the manufacturer's protocol. pTriEx4-Rac1-2G and pTriEx-RhoA-2G were a gift

675 RhoA-2G-control were constructed by deleting the coding sequence of acceptor Venus.
676 C1-mCitrine-FKBP-EZRabd(t567D), pCAG-Lyn11-FRB and YFP-FKBP were a gift from Tobias
677 Meyer (Addgene plasmid no. 155227, 155228, and 20175).
678 pLV[Exp]-Puro-CMV>mCherry/FKBP-EZRabd(t567d), pLV[Exp]-Puro-CMV>mCherry/FKBP and
679 pLV[Exp]-Puro-EF1A>Lyn-FRB-HA were constructed by VectorBuilder.

680 **Drug treatments**

681 Pharmacological inhibitors and chemical compounds were used at the following concentrations: 100
682 μM Cholesterol (Merck, #57-88-5), 100 μM MβCD (membrane domains inhibitor; Merck,
683 #128446-36-6). Rapamycin (MCE, #53123-88-9). Rapamycin was dissolved in DMSO for treatment
684 in cells (5 μM) and dissolved in 5.2% polyethylene glycol and 5.2%Tween-80 for treatment in mice
685 (2.0 mg/kg).

686 **Subcutaneous mouse xenograft model**

687 The mouse xenograft model was established by subcutaneous inoculation of 5×10^6 HeLa cells into
688 the suprascapular region of 6-week-old nude mice (10 per group). When tumors reached 100–200
689 mm^3 after 1 week, mice were randomly assigned to receive intraperitoneal injection of vehicle
690 (0.25 % polyethylene glycol, 0.25 % tween 80) or rapamycin (2 mg/kg) every other day. Tumors
691 were measured weekly using calipers and volume was calculated as $(\text{length}\times\text{width}^2)/2$. Mice were
692 euthanized after 2 weeks of treatment, and tumors were excised and fixed with 4%
693 paraformaldehyde.

694 **Immunofluorescence and histological analysis**

695 Cells grown on glass bottom or confocal dishes were fixed with 4% paraformaldehyde,
696 permeabilized with 0.1% Triton X-100 for 5 min. Cells were incubated with primary antibodies at
697 the optimal concentrations (according to the manufacturer's instructions) at 4 °C overnight.
698 Following three washes with PBS, samples were incubated with the appropriate secondary antibodies:
699 488/568/633 immunoglobulin G (IgG; H+L) and/or Alexa Fluor 568/647 phalloidin (Invitrogen) for
700 1 h at room temperature. Samples were again washed three times with PBS and mounted with

701 4',6-diamidino-2-phenylindole (DAPI, Invitrogen) for 10 min at room temperature. Confocal images
702 were taken on the Leica microscope. Experiments were replicated at least three times. Acquisition of
703 fluorescent images was carried out using a Leica TCS SP8 AOBS Confocal laser-scanning
704 microscope equipped with a 10×, 40×, or 63×objective (Leica, Germany).
705 Prior to embedding in paraffin, mouse tissues were fixed in 4% paraformaldehyde in PBS and
706 dehydrated. For histological analysis, 6 μm sections were cut and stained with Hematoxylin and
707 Eosin. For immunofluorescence analysis, 6 μm sections were incubated for 20 min in 10 mM sodium
708 citrate buffer, pH 6.0 at 90 °C to retrieve antigens on paraffin-embedded tissue samples. After 1 h
709 incubation in 5% fetal calf serum, sections were incubated overnight with diluted primary antibodies,
710 washed and further incubated for 2 h at room temperature with appropriate secondary antibodies.
711 Nuclei were stained with DAPI for 10 min at room temperature. Confocal images were obtained
712 using Leica microscope equipped with a 10×, 40×, or 63×objective. Experiments were replicated
713 at least three times.

714 **Cholera toxin subunit B (CTxB) staining**

715 HeLa cells were grown on 35 mm confocal dishes and cultured for 14 days. The cells were then
716 rinsed with cold Hank's balanced salt solution (HBSS)+0.5% BSA and incubated with 0.5 μg/mL
717 CFTM 488A or 633 conjugated CT-B in cold HBSS+0.5% BSA and incubated at 4°C for 30 minutes
718 in the dark. Cells were washed five times with cold HBSS+0.5% BSA and fixed in 4%
719 paraformaldehyde in PBS for 15 minutes at room temperature. Nuclei were stained with DAPI for 10
720 min at room temperature.

721 **Transwell invasion and migration assays**

722 For the Transwell invasion assay, briefly, 5-10 cells in 200 μL 10% FBS DMEM were reseeded into
723 the upper chamber of a 24-well Transwell of 8 μm pore size (Corning Inc., Corning, NY, USA) with
724 coated-Matrigel (BD Bioscience, San Jose, CA, USA), and 600 μL medium with 10% FBS was
725 loaded into the well below. After culture for 14 days, the upper chamber was replaced with
726 serum-free medium and later incubated at 37 °C for 48 h. Transwell insert membranes were fixed
727 with 4% paraformaldehyde and stained with DAPI. For the Transwell migration assay, all procedures

728 were similar but without the incubation of Matrigel. The percentage of migrating and invading cells
729 through the filter was imaged under a Leica SP8 Confocal microscope, and measured using the
730 ImageJ software.

731 **GelMA degradation assay**

732 Gelatin-Cy5 and Gelatin-FITC methacryloyl (GelMA, EFL-GM-90, China), lithium phenyl-2, 4,
733 6-trimethylbenzoylphosphinate (LAP), and a blue light source (3 W, 405 nm) were purchased from
734 Engineering for Life, Suzhou, China. GelMA was dissolved in PBS at 30% (w/v) containing 0.25%
735 (w/v) LAP. The mixture was transferred to a glass slide and exposed to blue light irradiation for 90 s
736 to crosslink the GelMA. Then the prepared hydrogels were rinsed with PBS three times, and then
737 a single cell was seeded on hydrogels in 24-well plates and cultured for 14 days. Cells were fixed
738 with 4% paraformaldehyde at room temperature for 15 min and washed three times with PBS. The
739 sample was incubated in 0.1% Triton X-100 for 10 min. Subsequently, the samples were stained for
740 actin with phalloidin for 60 min and stained for nuclei with DAPI for 10 min.

741 **RNA seq analysis**

742 HeLa cells were primed for 20 days in crowding or uncrowding culture, followed by exposure to
743 sparse culture for different times (0, 1, 3, or 10 days). The samples were collected and sent to the
744 Beijing Genomics Institute (BGI, China) for RNA sequencing performed on the BGISEQ-500
745 platform. The data was analyzed using Dr. Tom system multi-omics interactive system (BGI, China).
746 Q-value was obtained by false discovery rate (FDR) correction of the P-value. Differentially
747 expressed genes (DEGs) ($Q \leq 0.05$, $|\log2FC| \geq 1$) were analyzed by DEseq2 software. Volcano plot
748 visualization of gene expression patterns was performed using R and results with $Q \leqslant 0.05$ were
749 considered statistically significant.

750 **Atomic force microscopy (AFM)**

751 HeLa cells were grown on 35 mm confocal dishes and cultured for 14 days. Cell samples were fixed
752 with 4% paraformaldehyde, after washing cells with PBS to remove potential impurities on the cell
753 surface, and then kept in PBS. AFM experiment was performed in PBS buffer solution at room

754 temperature in PeakForce Tapping mode by scanning probe microscope Asylum MFP-3D-SA
755 (Asylum Research, USA). A PeakForce qp-BioAC probe (nominal spring constant 0.06-0.18 N/m,
756 Nanosensors, Neuchatel, Switzerland) was used to image the cell surface. The scanning parameters
757 were as follows: scan size of 30 μm, scan rate of 0.1 Hz, set point of 162.21 mV, integral gain of
758 611.37, drive amplitude of 2 V. All images were taken at a resolution of 256×256 pixels. The scan
759 area depended on the size of the HeLa cell and ranged from 30×30~50×50 μm^2. Image processing
760 and data analysis were performed by the Asylum MFP-3D-SA software.

761 **Focused ion beam and scanning electron microscopy**

762 The fixation of micropatterned HeLa cells was performed at room temperature for 15 minutes using
763 a 2.5% v/v glutaraldehyde (Electron Microscopy Sciences) solution in PB buffer. After washing the
764 samples three times with PB buffer, the samples were osmicated with 1% osmium tetroxide/1.5%
765 potassium ferricyanide in distilled water for 30 minutes. The samples were then washed three times
766 with distilled water and then dehydrated through a graded ethanol series. After dehydration, samples
767 were infiltrated with Pon 812 Resin (SPI) by incubating the samples in a diluted series of ethanol-
768 Pon 812 at a 1:1, 1:2, and 1:3 ratio for 1 hour for each, followed by overnight in pure resin. The pure
769 resin was changed once in the first hour, then the samples were incubated in an oven at 60 °C for 48
770 hours. 70 nm sections were cut by ultramicrotome (Leica EM UC7) and stained with uranyl acetate
771 (UA) and lead citrate, then imaged by TEM. To visualize the cell surface, the resin covering the cell
772 was removed using acetone, and the cells filled with resin were polymerized at 60 °C for 48 hours.
773 10nm gold was coated before imaged by SEM. After that, resin was re-applied, and 70 nm Cross
774 section of the cells were cut for TEM imaging.

775 **Laplace pressure calculation**

776 Laplace pressure measurements were conducted using the 900A micro pressure system (WPI) based
777 on the servo-null method, following the manufacturer's instructions. A microelectrode was created
778 from a glass capillary (0.75 mm inner diameter/1.0 mm outer diameter) using a micropipette puller
779 (PC-100, Narishige). The one-stage pull mode was employed with the following settings: Heat 50V,
780 Weights: 250 g. Before the measurement, the microelectrode was calibrated using the calibration

781 chamber and pressure source. The microelectrode was filled with a 1M NaCl solution, while the
782 calibration chamber contained a 0.1M NaCl solution. To perform the measurements, the
783 microelectrode was mounted to a piezo-driven xyz micromanipulator (SN-PCZ-50R, WPI) located in
784 an environmental chamber (37 °C, 5% CO2). A four-channel AD converter was used to record the
785 pressure signal. The microelectrode tip was inserted into the cells at a 45-degree angle and then
786 slightly retracted to release compression on the cells. This position was maintained for at least 10
787 seconds, and the Laplace pressure was determined as the average pressure during this this period.

788 **Membrane tension measurements**

789 Cell membrane tension was measured using Flipper-TR fluorescent tension probe (SC020,
790 Cytoskeleton, Inc.). HeLa cells were cultured on the gelatin-coated 35 mm confocal dishes for 14
791 days until the cell sheet was formed. Cells were then treated with 1 mM Flipper-TR at 37 °C for 15
792 minutes to achieve appropriate labeling prior to imaging. The fluorescence lifetime of Flipper-TR
793 was measured by using an Olympus fluorescence lifetime imaging microscope (FLIM, FV-1200,
794 Japan). Excitation was performed using a pulsed 488-nm laser operating at 40 MHz, and the
795 emission signal was collected through a 550-650-nm bandpass filter using a HyD SMD detector.
796 Lifetimes of Flipper-TR were extracted from FLIM images using SymPhoTime 64 software
797 (PicoQuant).

798 **Fluorescence resonance energy transfer (FRET)**

799 HeLa cells were cultured on the gelatin-coated 35 mm confocal dishes for 14 days and transfected
800 with genetically encoded biosensors expressing Rac1-2G-control, Rac1-2G, RhoA-2G, or
801 RhoA-2G-control. After 48 hours, acquisition of fluorescent images and FRET experiments were
802 carried out using an Olympus FV-1200 Confocal laser-scanning microscope. Argon laser lines of 458
803 nm and 514 nm were used to excite mTFP1 and mVenus fluorophores, which represent the donor and
804 the acceptor, respectively. For proper image recording, a HyD SMD detector was employed by
805 gating a spectral acquisition window of 486-502 nm for the donor and 524-600 nm for the acceptor.
806 FRET analysis was performed using SymPhoTime 64 software (PicoQuant) and FRET efficiency
807 was calculated: 1-τdonor, Rac1 or Rhoa-2G /τdonor, Rac1 or Rhoa-2G-control.

808 **Molecular dynamics (MD) simulations**

809 In this work, CHARMM-GUI webserver[53], Martini coarse-grained force field[52] and GROMACS
810 software[76] (version 2019.6) were used to perform all MD simulations to capture the phase separation
811 processes of three-component lipid vesicles with different radii (10 nm and 20 nm).
812 1,2-dipalmitoyl-sn-glycero-3-phosphocholine (DPPC),1,2-dilinoleoyl-sn-glycero-3-phosphocholine
813 (DUPC), and cholesterol (CHOL) with the molar ratio of 5:3:2 was adapted to construct the lipid
814 vesicles for studying the kinetics of model membrane domains[77,78]. For all simulations, a standard 1.2
815 nm cutoff was applied for van der Waals interactions, and the LJ potential was shifted to zero
816 smoothly from 0.9 to 1.2 nm to reduce the cutoff noise. For columbic potential, a 1.2 nm cutoff was
817 used for short-range electrostatic interactions, with a smooth shift to zero from 0 to 1.2 nm. The
818 neighbor list for nonbonded interactions was updated every 10 steps with a cut-off of 1.2 nm.
819 Periodic boundary conditions were applied in all three dimensions. All simulations were run for 5 μs
820 with the time step of 20 fs under the isothermal-isobaric (NPT) ensemble. Snapshots and movies
821 were rendered by VMD[79].

822 **Monte carlo (MC) simulations**

823 We employ the Monte Carlo (MC) method to investigate the response of a discretized membrane,
824 containing membrane domains and interacting with cortical actin via transmembrane proteins, to the
825 pressure and membrane tension. The system Hamiltonian consists of membrane elastic energy,
826 protein-cytoskeleton binding energy, as well as raft-raft contact energy. The system configuration
827 evolves through three types of trial moves including vertical displacements of membrane patches,
828 lateral translations of proteins, and lateral shifts of raft patches. These trial moves are accepted or not
829 according to the Metropolis algorithm. We perform simulations with membrane size up to 500 nm ×
830 500 nm, and all parameters used in the simulations are sourced from exiting literatures. For a more
831 detailed description, see our Supplementary Materials.

832 **Quantification and statistical analysis**

833 Statistical analyses for all experiments were performed using Prism (GraphPad) v5.02. Statistical
834 data are presented as median or mean ± SEM or SD. Statistical tests used and p values are specified

in the figure legends. Samples in most cases were defined as the number of cells counted/examined across multiple different fields of view on the same dish/slide, and represent data from a single sample within a single experiment, which are representative of at least three additional independently conducted experiments.

Reporting summary

Further information on research design is available in the Nature Research Reporting Summary linked to this paper.

Data availability

All RNA-sequencing data from this study have been deposited in the Gene Expression Omnibus (https://www.ncbi.nlm.nih.gov/geo/) under accession code GSE281770. All other data in the manuscript, supplementary materials, source data and custom code are available from the corresponding author upon reasonable request. Source data are provided with this paper.

ACKNOWLEDGMENTS

We thank Professor Dake Zhang (Beihang University) for technical assistance with RNA-seq analysis. This work was supported by the National Natural Science Foundation of China (NSFC) (12222201, 82273500, 82372750), the Beijing Natural Science Foundation (L248062), the National Key R&D Program of China (2023YFC2507000, 2017YFA0506500), Fundamental Research Funds for the Central Universities (ZG140S1971, KG16301601) and the CAMS Innovation Fund for Medical Sciences (2023-I2M-3-003 and 2022-I2M-1-008).

AUTHOR CONTRIBUTIONS

J. D., Y.B.F., and Y.Z. designed and supervised the experiments. X.B.Z., M.T., Z.K.L., Z.G., and T.L.C. performed the experiments. M.T. and B.Q.S. performed the mouse xenograft assays. X.H.W. performed Laplace pressure assay. S.H. performed Cy5-conjugated gelatin hydrogels preparation.

L.L., and X.B.L. developed the computational model. J.H.F. and S.J.W. performed patient tumor samples preparation. All the authors took part in the data analysis. X.B.Z. and J.D. interpreted the data and wrote the paper.

COMPETING INTERESTS

The authors declare no competing interests.

FIGURES

Fig. 1.

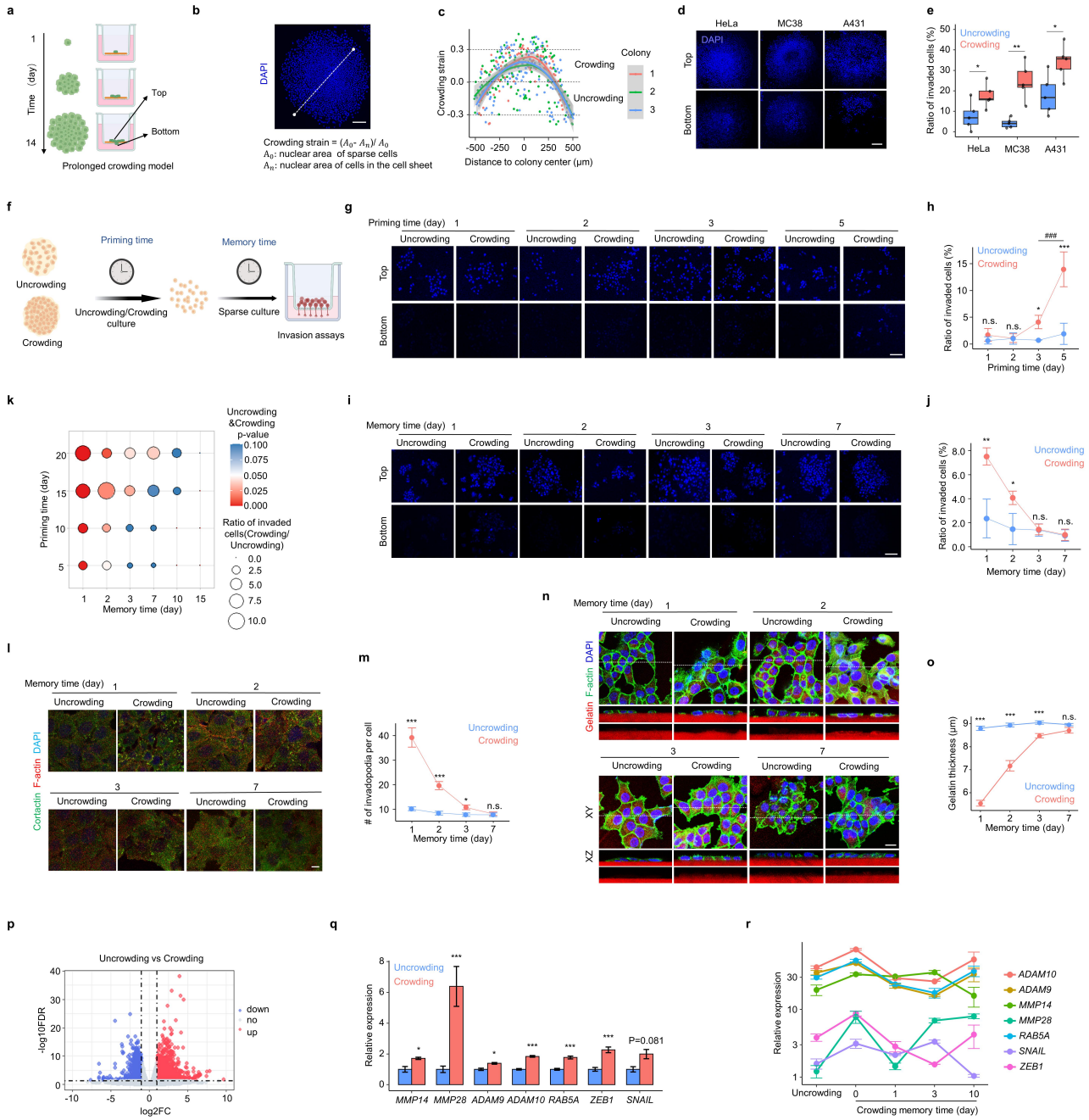

Figure 1. Prolonged crowding initiates cancer cell invasion with mechanomemory. (**a**) Schematic diagram of prolonged crowding-induced cell invasiveness model. (**b**) Quantitation of the individual cell nucleus area as crowding strain along the lines in the panel. Scale bar: 200 μm. (**c**) The statistical analysis of crowding strain per cell along the panel lines (b). The cell sheet was segmented into crowding (crowding strain from 0 to 0.3) and uncrowding (crowding strain from -0.3 to 0). (**d**) Transwell matrigel invasion assay of a growing monoclonal HeLa, MC38, and A431 cell sheets after culture for 14 days. Representative DAPI images of cells that accumulated on the top (uninvaded) and bottom (invaded) surface of the insert membranes. Scale bar: 200 μm. (**e**) The ratio

of invaded cells in uncrowded and crowded HeLa, MC38, and A431 cells. (**f**) Schematic illustration of the experimental procedure to test the invasion of HeLa cells after priming time for uncrowding and crowding culture and memory time for sparse culture. (**g**) Transwell matrigel invasion assay of HeLa cells after experiencing uncrowding and crowding for 1, 2, 3, 5 days (priming time), subsequently collected and transferred to transwell chamber for 48 hrs. Representative DAPI images of cells that accumulated on the top and bottom surface of the insert membranes. Scale bar: 100 μm. (**h**) The ratio of invaded cells in uncrowded and crowded HeLa cells in panel (g). (**i**) HeLa cells were grown dishes in crowding or uncrowding culture for 5 days, transferred to new dishes for 1, 2, 3, 7 days (memory time), subsequently collected and transferred to transwell chamber for 48 hrs. Representative DAPI images of cells that accumulated on the top and bottom surface of the insert membranes. Scale bar: 100 μm. (**j**) The ratio of invaded cells in uncrowded and crowded HeLa cells in panel (i). (**k**) The correlation graph between priming time and memory time in cell culture for invasion analysis. (**l**) HeLa cells were grown dishes in crowding or uncrowding culture for 5 days, transferred to matrigel-coated dishes for 1, 2, 3, 7 days. Representative XY slice image of cortactin distribution at the basal membrane in uncrowding/crowding groups. Scale bar: 10 μm. (**m**) Quantification of invadopodia number per cell with corresponding memory time. (**n**) HeLa cells were grown dishes in crowding or uncrowding culture for 5 days, transferred to Cy5-conjugated gelatin hydrogels for 1, 2, 3, 7 days. Representative XY slice image of F-actin staining in uncrowding/crowding groups. Scale bar: 20 μm. (**o**) Quantification of correlation between Cy5-conjugated gelatin thickness underneath cells and its memory time. (**p**) The volcano plot shows deferentially expressed genes between uncrowding and crowding. Each dot represents a gene; genes in red are up, genes in blue are down-regulated. (**q**) Boxplots showing mRNA expression data for *MMP14*, *MMP28*, *ADAM9*, *ADAM10*, *RAB5A*, *ZEB1*, and *SNAIL* in uncrowded and crowded HeLa cells as determined by RNA seq data respectively. (**r**) Relative expression of *MMP14*, *MMP28*, *ADAM9*, *ADAM10*, *RAB5A*, *ZEB1*, and *SNAIL* in HeLa cells after experiencing uncrowding or crowding for 0, 1, 3, 10 days (memory time). Schematic images (c, f) were created with BioRender.com. Data are presented as mean ± SEM; *$p < 0.05$, **$p < 0.01$, ***$p < 0.005$, not significant (n.s.); two-tailed unpaired t-test.

Fig. 2.

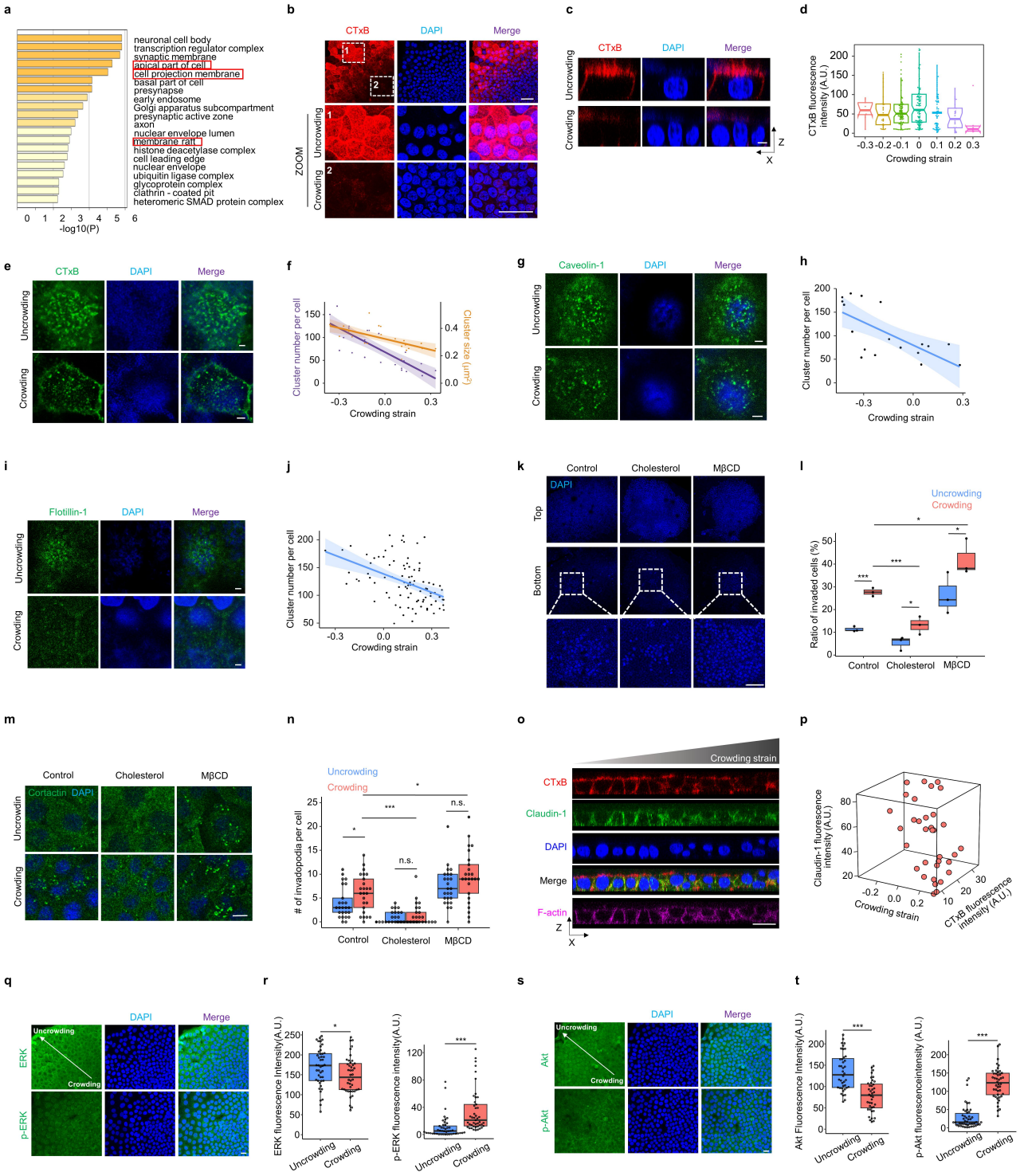

Figure 2. Prolonged crowding promotes cancer cell invasiveness by disrupting the aggregation of membrane domains. (**a**) The Gene Ontology (GO) cellular components enriched by Metascape from RNA sequencing data. (**b**) Representative XY confocal images for CTxB staining in uncrowded and crowded HeLa cells. Scale bar: 50 μm. (**c**) Reconstructed XZ confocal images for CTxB staining at the apical membrane of uncrowded and crowded HeLa cells. Scale bar: 5 μm. (**d**) Quantitation of correlation between CTxB fluorescence intensity per cell and its crowding strain. (**e**) Representative XY confocal images for CTxB staining at the apical membrane of uncrowded and crowded HeLa

cells. Scale bar: 2 μm. (**f**) Quantitation of correlation between the number and size of CTxB clusters per cell and its crowding strain. (**g**) Representative XY confocal images showing immunostaining for Caveolin-1 at the apical membrane of uncrowded and crowded HeLa cells. Scale bar: 2 μm. (**h**) Quantitation of correlation between the number of Caveolin-1 clusters per cell and its crowding strain. (**i**) Representative XY confocal images showing immunostaining for Flotillin-1 at the apical membrane of uncrowded and crowded HeLa cells. Scale bar: 2 μm. (**j**) Quantitation of correlation between the number of Flotillin-1 clusters per cell and its crowding strain. (**k**) Representative XY slice images of cholesterol- and MβCD-treated HeLa cell sheets by Transwell invasion assay. Scale bar: 100 μm. (**l**) Quantification of invaded cell number in panel (k). (**m**) Representative XY slice images showing immunostaining for cortactin in uncrowded and crowded cells treated with cholesterol and MβCD. Scale bar: 10 μm. (**n**) Quantification of invadopodia density per cell in panel (m). (**o**) Reconstructed XZ confocal images showing the localization of CTxB and Claudin-1 in the regions with different crowding strain. Size bars: 20 μm. (**p**) Quantitation of correlation between Claudin-1 fluorescence intensity and CTxB fluorescence intensity in differently crowded cells. (**q**) Representative XY confocal images showing immunostaining for ERK and p-ERK in uncrowded and crowded HeLa cells. Scale bar: 2 μm. (**r**) Quantification of fluorescence intensity of ERK and p-ERK per cell in panel (q). (**s**) Representative XY confocal images showing immunostaining for Akt and p-Akt in uncrowded and crowded HeLa cells. Scale bar: 20 μm. (**t**) Quantification of fluorescence intensity of Akt and p-Akt per cell in panel (s). Data are presented as $*p < 0.05$, $***p < 0.005$; two-tailed unpaired t-test.

Fig. 3.

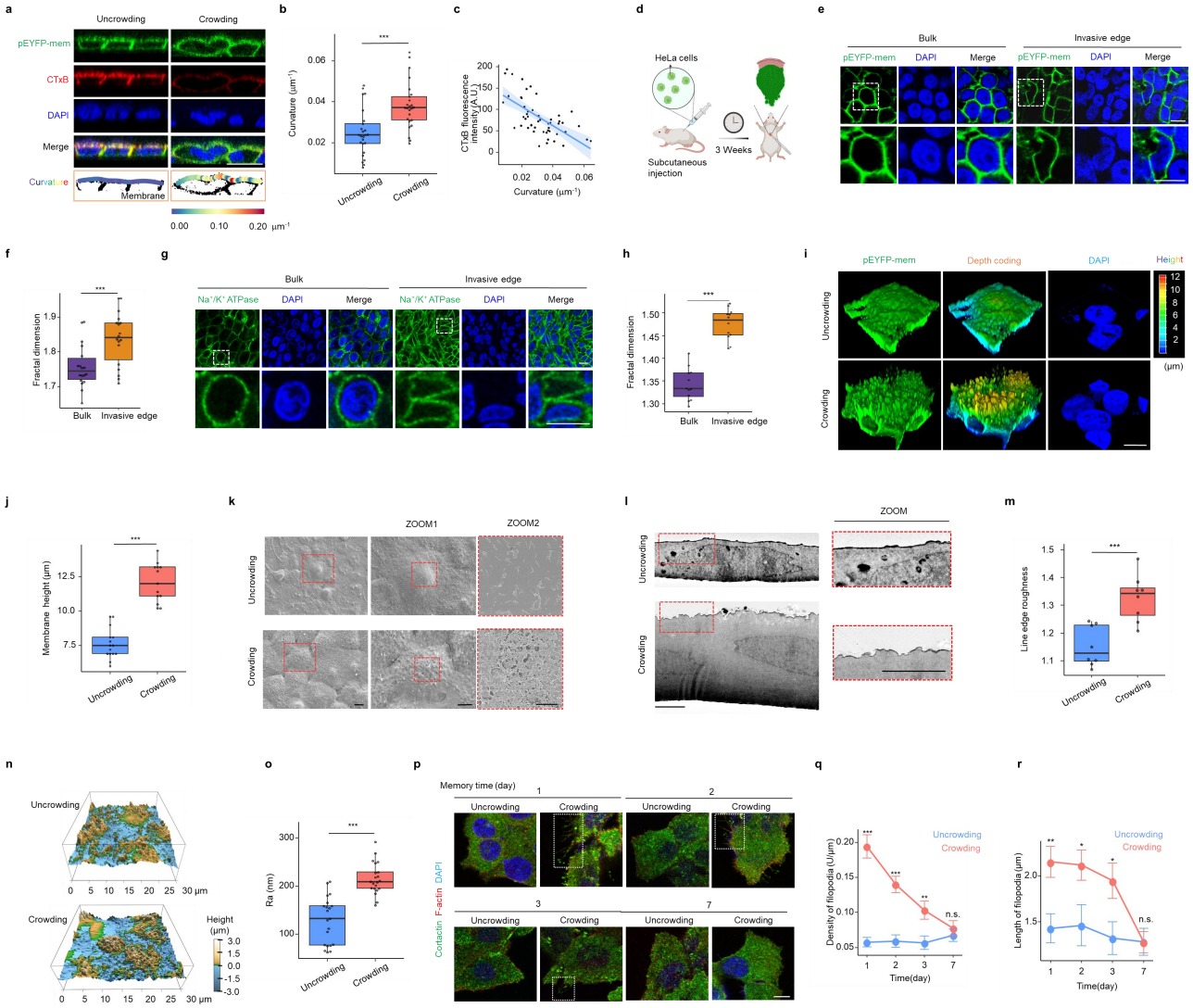

Figure 3. Prolonged crowding triggers a nSCTT of plasma membranes. (**a**) Reconstructed XZ confocal images showing CTxB level and membrane curvature using ImageJ and plugin Kappa in uncrowded and crowded HeLa cells expressing pEYFP-mem. Scale bar: 20 μm. (**b**) Quantitation of membrane curvature in uncrowded and crowded HeLa cells in panel (a). (**c**) Quantitation of correlation between CTxB fluorescence intensity and membrane curvature in panel (a). (**d**) Schematic diagram of subcutaneous nude mouse xenograft model using EYFP-mem+ HeLa cells. After 3 weeks of tumor growth, mouse tissues were harvested and tumor architectures were analyzed for the indicated parameters. (**e**) Representative XY slice image of pEYFP-mem from bulk and invasive edge of nude mouse xenografts. Scale bar: 10 μm. (**f**) Quantitation of correlation between fractal dimension per cell from bulk and invasive edge of nude mouse xenografts. (**g**) Representative XY slice image of sodium potassium ATPase in the uncrowded and crowded regions of human skin cancer tissues. Scale bar: 10 μm. (**h**) Quantitation of correlation between fractal dimension and crowding strain per cell in human skin cancer tissues. (**i**) Confocal 3D reconstruction of the apical membrane of uncrowded and crowded HeLa cells expressing pEYFP-mem. Scale bar: 10 μm. (**j**) Quantitation of membrane height in uncrowded and crowded HeLa cells. (**k**) Scanning electron

microscopy (SEM) images of plasma membranes in uncrowded and crowded HeLa cells. Scale bar: 10 and 5 μm. (**l**) Transmission Electron Microscope (TEM) images of apical plasma membranes revealing the presence of membrane bending in the range of 100 – 500 nm. Scale bar: 5 μm. (**m**) Quantification of line edge roughness in uncrowded and crowded HeLa cells (l). (**n**) The topographic images of HeLa cells by AFM showing the height distribution of the membrane with the size of 30 μm × 30 μm. For uncrowded cells, the surface of membrane was relatively flat. More protruding structures were observed in crowded cells. (**o**) Average roughness (Ra) of the apical plasma membrane was analyzed from 3×3 μm frame ultrastructure images by AFM. (**p**) Representative XY slice image of cortactin distribution in HeLa cells after uncrowding/crowding culture for 5 days and sparse culture for 1,2,3,7 days. Scale bar: 10 μm. (**q, r**) Quantification of filopodia density and length per cell with corresponding memory time in panel (p). Data are presented as mean ± SEM; *$p < 0.05$, **$p < 0.01$, ***$p < 0.005$; two-tailed unpaired t-test.

Fig. 4.

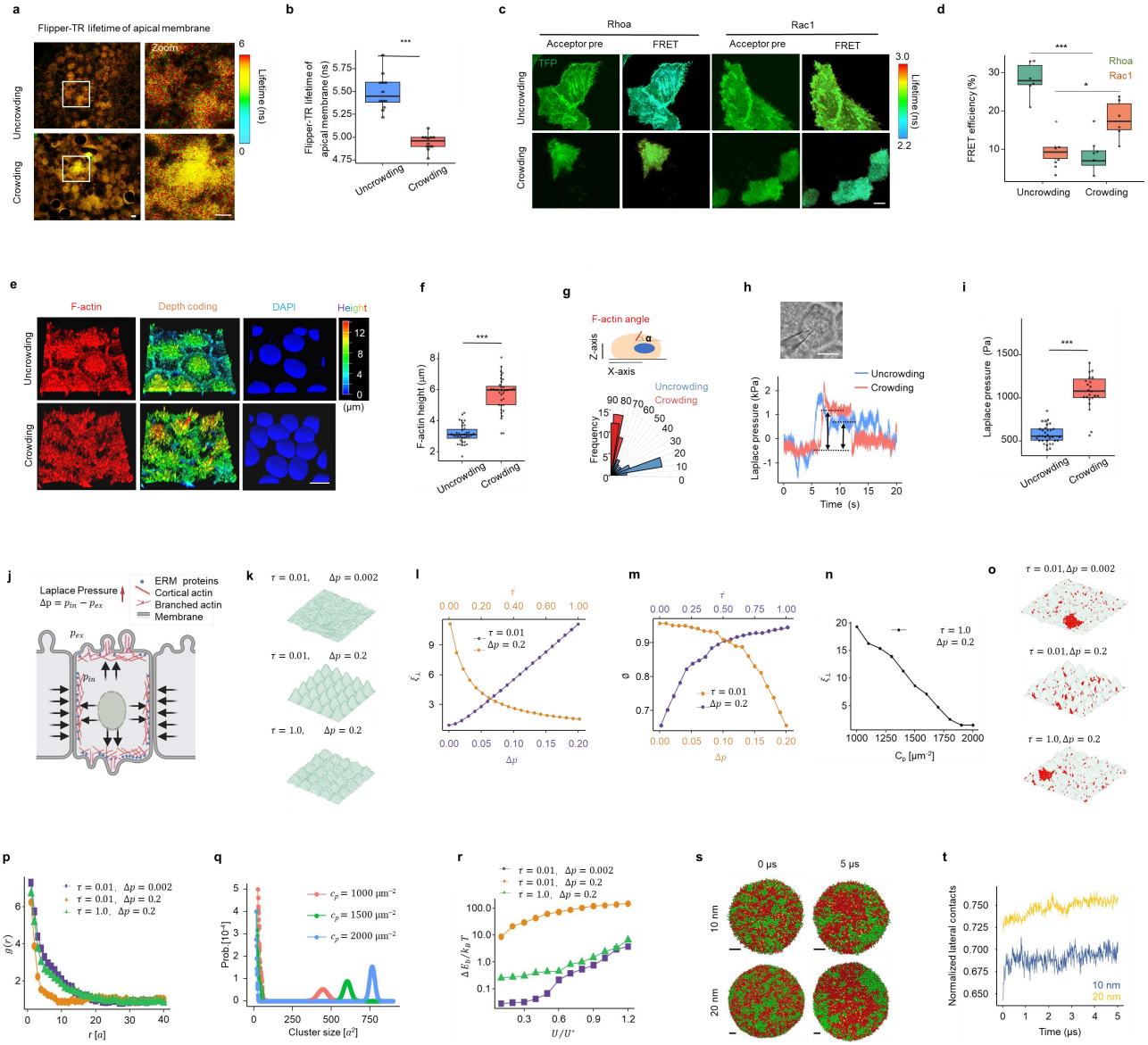

Figure 4. Prolonged crowding triggers nSCTT and disrupts membrane domains by increasing Laplace pressure. (**a**) Representative FLIM images of Flipper-TR lifetime values to analyze membrane tension in uncrowded and crowded cells. Color scale from 0 to 6 ns. Scale bars: 10 μm. (**b**) Quantification of the average lifetime of Flipper-TR from full images. Data are presented as boxplot. (**c**) FRET analysis of uncrowded and crowded HeLa cells expressing the RhoA or Rac1 biosensor. Representative confocal images of over-expressed cells before photobleaching (acceptor pre) are shown. Representative FLIM images of photobleaching in uncrowded and crowded cells are shown. Color scale represents the range of FRET efficiency. Scale bar: 10 μm. (**d**) Quantitation of the fluorescence increase (% FRET efficiency) of RhoA and Rac1 upon photobleaching in uncrowded and crowded cells. Data are presented as boxplot. (**e**) Confocal 3D reconstruction of the apical side of uncrowded and crowded HeLa cells stained for F-actin. Scale bar: 10 μm. (**f**) Quantification of the average height of F-actin from the apical side in uncrowded and crowded cells. (**g**) Actin angle distribution data for cells experiencing uncrowding and crowding displayed as a rose

plot in which the absolute value of the angles was compared. (**h**) Quantifying Laplace pressure in uncrowded and crowded HeLa cells using a micro-pressure probe. The baseline reading is close to zero when the microelectrode is not in contact with the cells. A transient pressure spike is recorded as the tip of the microelectrode penetrates the membrane. This is followed by a stable reading for about 5-10 s, before some potential leaks occur, which may cause a gradual drop in the reading with time. Scale bar: 10 μm. (**i**) Quantification of the Laplace pressure of cells experiencing uncrowding and crowding. (**j**) Schematic diagram representing how the increased Laplace pressure controls the protrusions of plasma membranes due to the cellular squeeze of each other. (**k**) Snapshot from Monte Carlo simulations of nanoscale topography of plasma membranes with different membrane tension $\bar{\tau} = \tau a^2 / \kappa$ and Laplace pressure $\Delta\bar{p} = \Delta p a^3 \left(\kappa k_B T\right)^{-1/2}$. (**l**) The rescaled roughness $\bar{\xi}_\perp = \xi_\perp \left(\kappa / k_B T\right)^{1/2} / a$ as a function of membrane tension and Laplace pressure. (**m**) The ratio of linker proteins ϕ that bound to the cortical actin as a function of Laplace pressure and membrane tension. (**n**) The rescaled roughness as a function of the density of linker proteins C_p that bound to cortical actin. (**o**) Snapshot from Monte Carlo simulations for aggregation of membrane domains for different membrane tension and Laplace pressure as indicated in each figure. (**p**) Pair distribution function g (r) of membrane domains as a function of the distance r for different membrane tension and Laplace pressure as indicated in this figure. (**q**) The probability of cluster size for membrane domains with different density of linker proteins C_p that bound to cortical actin. (**r**) The changes of bending energy as a function of the raft-raft contact energy. (**s**) Snapshots of DPPC (red) / DUPC (green) / CHOL (yellow) liposomes with different inner radius at 0 and 5 μs. Scale bar: 4 nm. (**t**) Time evolution of normalized lateral contacts of DUPC lipids for different systems. Data are presented as *$p < 0.05$, ***$p < 0.005$; two-tailed unpaired t-test.

Fig. 5.

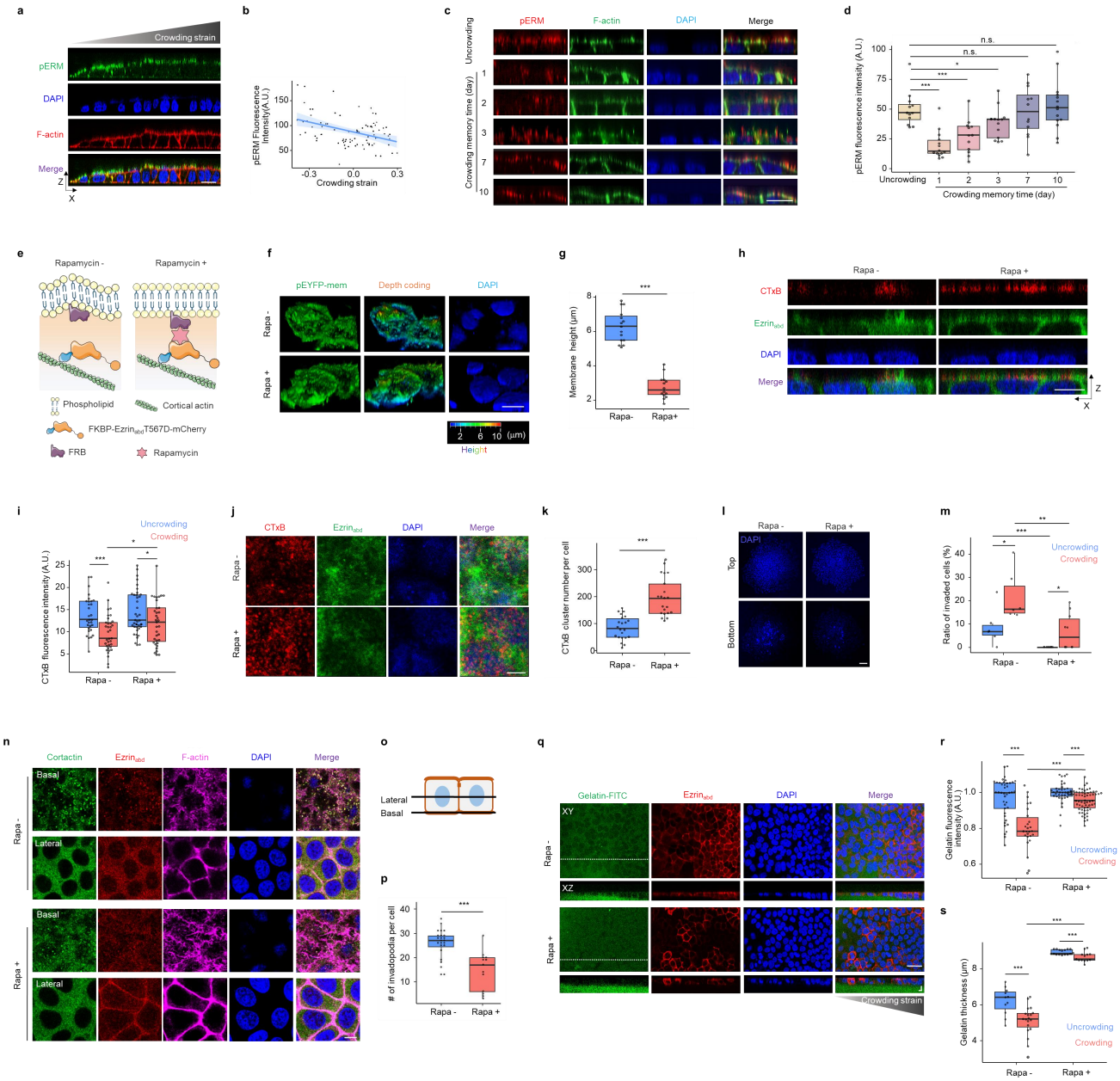

Figure 5. Suppressing the pressure-sensation of membrane domains inhibits crowding-initiated cancer cell invasiveness. (**a**) Reconstructed XZ confocal images of pERM localization at the apical side in uncrowded and crowded HeLa cells. Scale bar: 20 μm. (**b**) Quantification of pERM fluorescence intensity per cell with corresponding crowding strain. (**c**) Reconstructed XZ confocal images of pERM localization at the apical side of HeLa cells after uncrowding/crowding culture for 5 days and sparse culture for 1, 2, 3, 7, 10 days. Scale bar: 20 μm. (**d**) Quantification of pERM fluorescence intensity with corresponding memory time from uncrowded and crowded groups. (**e**) Schematic diagram for a FKBP-EzrinabdT567D construct to acutely increase cortical actin by recruitment of the EzrinabdT567D to the plasma membranes after rapamycin treatment. (**f**) Confocal 3D reconstruction of the apical membrane of FKBP-EzrinabdT567D-mCherry+; EYFP-mem+ HeLa cells treated with rapamycin or vehicle. Scale bar: 10 μm. (**g**) Quantification of the average height of

membrane from the apical side in control and rapamycin treated cells. (**h**) Reconstructed XZ confocal images showing CTxB fluorescence intensity in FKBP-EzrinabdT567D-mCherry+ HeLa cell sheets treated with rapamycin or vehicle. Scale bar: 10 μm. (**i**) Quantitation of CTxB fluorescence intensity in uncrowded and crowded cells treated with rapamycin or vehicle. (**j**) Representative XY confocal images of CTxB staining at the apical membrane of FKBP-EzrinabdT567D-mCherry+ HeLa cell sheets treated with rapamycin or vehicle. Scale bar: 5 μm. (**k**) Quantitation of the number of CTxB cluster per cell treated with rapamycin or vehicle. (**l**) Transwell matrigel invasion assay of FKBP-EzrinabdT567D-mCherry+ HeLa cell sheets after treatment with rapamycin or vehicle. Representative DAPI images of cells that accumulated on the top (uninvaded) and bottom (invaded) surface of the insert membranes. Scale bar: 100 μm. (**m**) Ratio of invaded cells in FKBP-EzrinabdT567D-mCherry+ HeLa cell sheets treated with rapamycin or vehicle in panel (l). (**n**) Representative XY slice image of cortactin and F-actin staining in FKBP-Ezrinabd T567D-mCherry+ HeLa cell sheets treated with rapamycin or vehicle. Scale bar: 10 μm. (**o**) Schematic diagram of lateral and basal cross-sections in HeLa cell sheets. (**p**) Quantification of invadopodia density per cell in control and rapamycin groups in panel (n). (**q**) FKBP-EzrinabdT567D-mCherry+ HeLa cells were plated on FITC-conjugated gelatin hydrogels. Representative XY and XZ slice images of gelatin-FITC and EzrinabdT567D-mCherry in cell sheets after rapamycin treatment. Scale bar: 10 μm. (**r, s**) Quantification of Cy5-conjugated gelatin fluorescence intensity and thickness in uncrowded and crowded cells treated with rapamycin or vehicle in panel (q). Data are presented as $*p < 0.05$, $**p < 0.01$, $***p < 0.005$; two-tailed unpaired t-test.

Fig. 6.

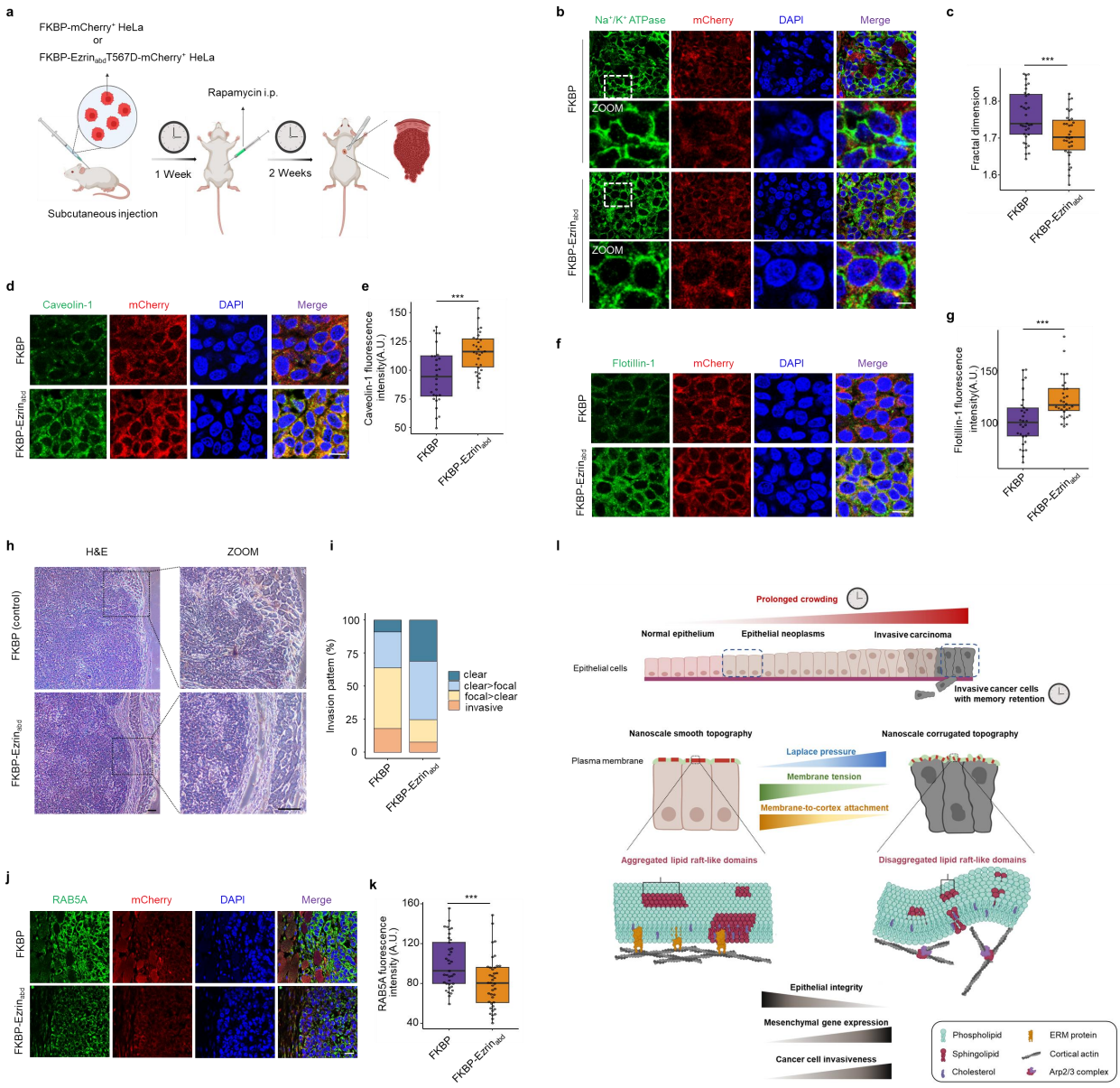

Figure 6 Suppressing the pressure-sensation of membrane domains inhibits tumor invasion in a mouse xenograft model. (**a**) Schematic diagram of subcutaneous nude mouse xenograft model using FKBP-Ezrin$_{abd}$T567D and FKBP (Control) over-expressed HeLa cells. After 1 week of tumor growth, mice were treated with rapamycin via i.p. three times per week. Tissues were harvested and tumor architectures were analyzed for the indicated parameters. (**b**) Representative XY slice images of sodium potassium ATPase and mCherry in mouse xenograft treated with rapamycin. Scale bar: 5 μm. (**c**) Quantitation of fractal dimension of HeLa cells expressed FKBP-Ezrin$_{abd}$T567D and FKBP in mouse xenografts. (**d**) Immunofluorescence analysis of Caveolin-1 in mouse xenografts treated with rapamycin. Scale bar: 10 μm. (**e**) Quantification of Caveolin-1 fluorescence intensity of tumor cells in panel (d). (**f**) Immunofluorescence analysis of Flotillin-1 in mouse xenografts treated with rapamycin. Scale bar: 10 μm. (**g**) Quantification of Flotillin-1 fluorescence intensity of tumor cells in panel (f). (**h**) Representative images of HE

`

staining in mouse xenografts treated with rapamycin. scale bar: 100 µm. (**i**) Invasion pattern of mouse xenografts in panel (h). Invasion was classified as “clear” (distinct border between muscle and tumor), “clear>focal” (more clear borders than areas with focal invasions), “focal>clear” (more focal invasions than clear borders), or “invasive” (no clear borders). Percentages of each category are given. Only samples with sufficient surrounding muscle tissue were evaluated. (**j**) Immunofluorescence analysis of RAB5A and mCherry in mouse xenografts treated with rapamycin, scale bar: 20 µm. (**k**) Quantification of RAB5A fluorescence intensity in the invasive edge of tumor in mouse xenografts. (**l**) Schematic diagram of pressure-sensing membrane domains triggered by prolonged crowding driving cancer cell invasiveness. The supported membrane consists of non-membrane domains containing unsaturated phospholipids and lipid membrane domains by association of sphingolipid and cholesterol molecules. Under uncrowded conditions, aggregated membrane domains reside in nanoscale smooth topography, maintaining a flat plasma membrane sustained by membrane-to-cortex attachment. In contrast, under prolonged crowding conditions, membrane domains become disaggregated are confined to regions with nanoscale corrugated topography with plasma membrane protrusions. This transition in membrane domain organization and topography is critical for driving cancer cell invasiveness. Schematic images (a, l) were created with BioRender.com Data are presented as ***$p < 0.005$; two-tailed unpaired t-test.

`

SUPPLEMENTAL FIGURES

Fig. S1.

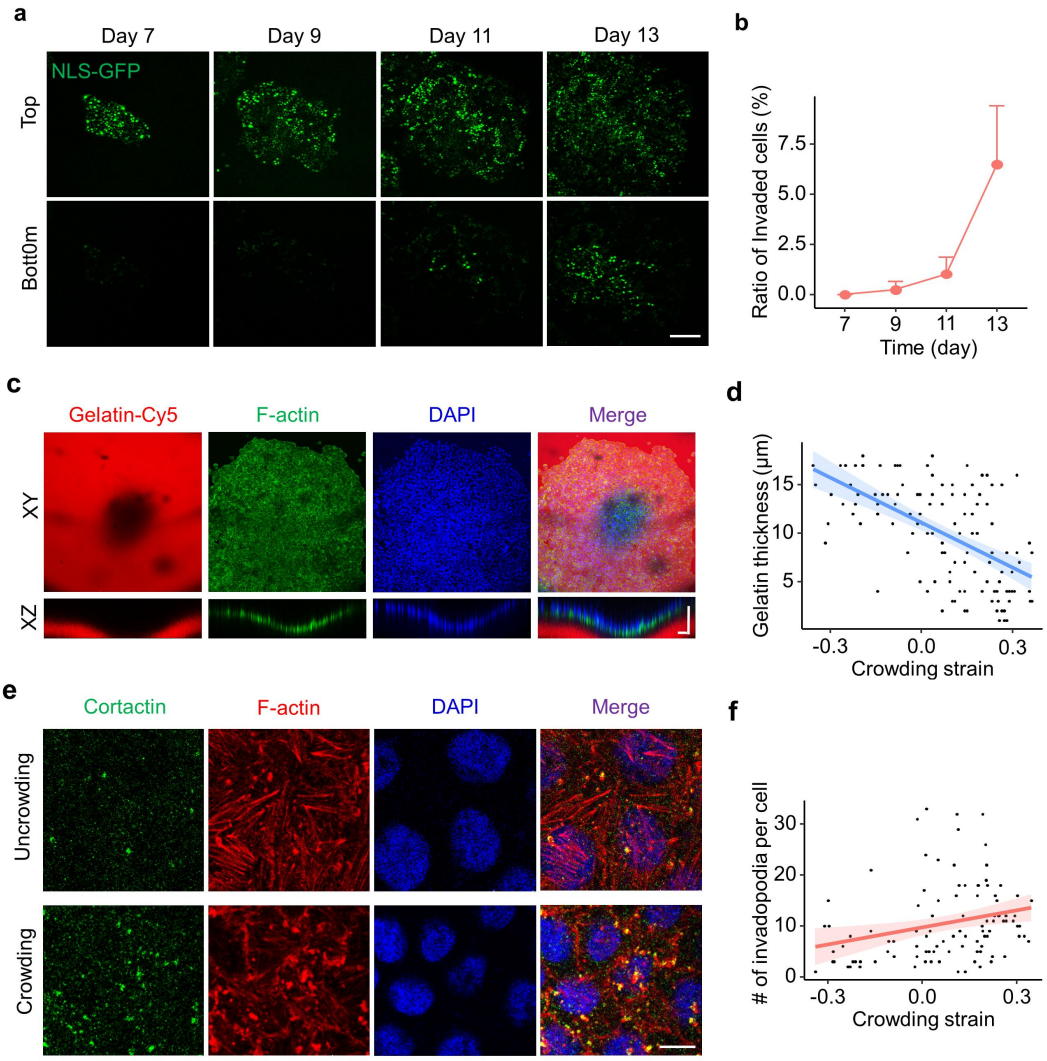

Fig. S1. Prolonged crowding drives cancer cell invasiveness. (**a**) Transwell matrigel invasion assay in a growing monoclonal NLS-GFP^{+} HeLa cell sheets captured for 7, 9, 11, 13 days after seeding. Representative DAPI images of cells that accumulated on the top and bottom surface of the insert membranes. Scale bar: 200 μm. (**b**) The ratio of invaded NLS-GFP^{+} HeLa cells was analyzed in panel (a). (**c**) HeLa cells were plated on Cy5-conjugated gelatin hydrogels for a growing monoclonal cell sheet. F-actin was stained with phalloidin. Scale bar: 50 μm. (**d**) Quantification of correlation between Cy5-conjugated gelatin thickness underneath cells and its crowding strain in panel (c). (**e**) Representative XY slice images of cortactin and F-actin staining in uncrowded and crowded cells. Scale bar: 10 μm. (**f**) Quantification of correlation between invadopodia density per cell and corresponding crowding strain in panel (e).

Fig. S2.

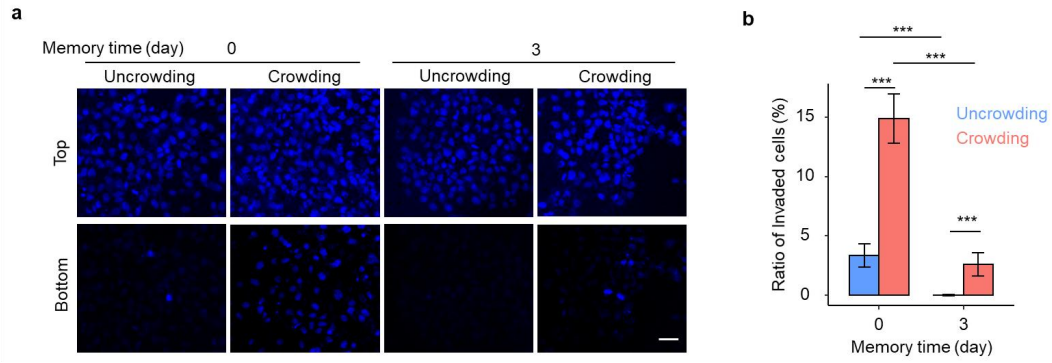

Fig. S2. Prolonged crowding drives A431 cell invasiveness with memory retention. (**a**) Transwell matrigel invasion assay of A431 cells after uncrowding/crowding culture for 5 days and sparse culture for 0 and 3 days. Representative DAPI images of cells that accumulated on the top and bottom surface of the insert membranes. Scale bar: 50 μm. (**b**) The ratio of invaded cells in uncrowded and crowded A431 cells in panel (a). Data are presented as mean ± SEM; ***$p < 0.005$; two-tailed unpaired t-test.

1118 **Fig. S3**

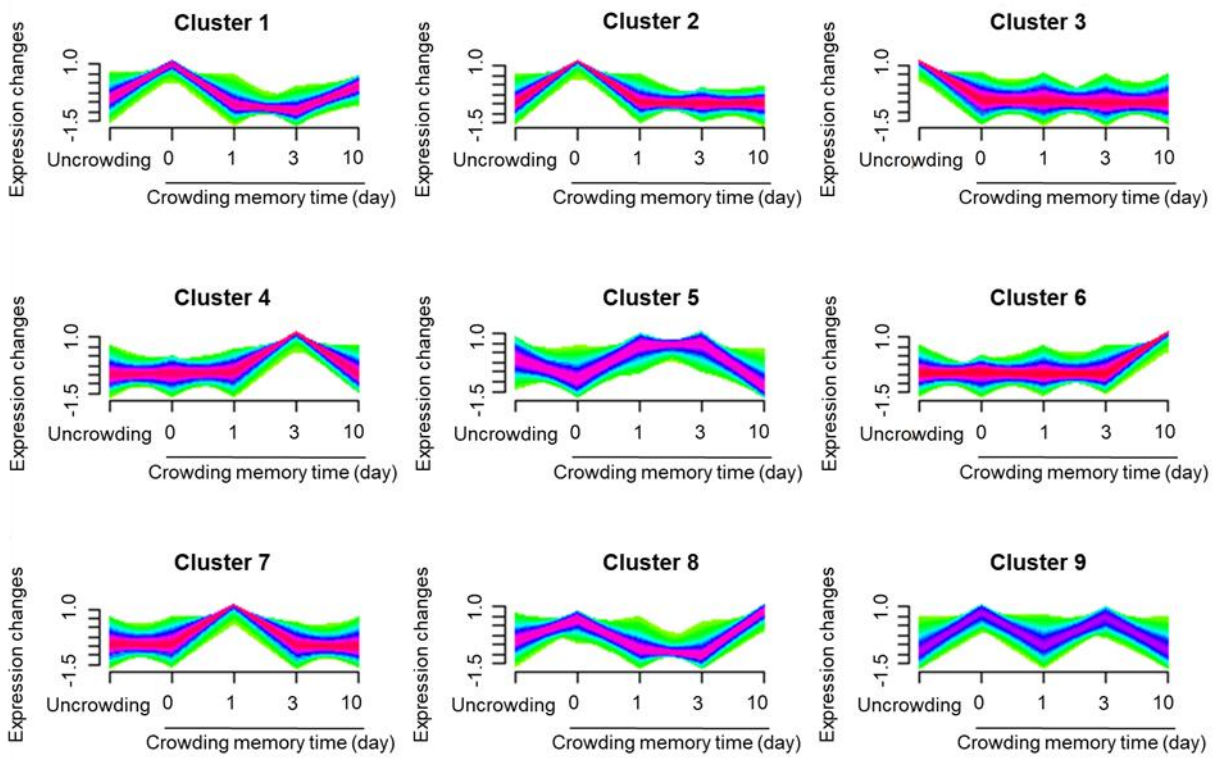

1119

1120 **Fig. S3. Identification of gene expression clusters in cells cultured under crowded or**
1121 **uncrowded conditions.** Cells were primed for 20 days in crowding or uncrowding culture,
1122 followed by exposure to sparse culture for different times (0, 1, 3, or 10 days). 34,520 genes were
1123 clustered using mFuZz into significant discrete clusters.

1124

`

Fig. S4.

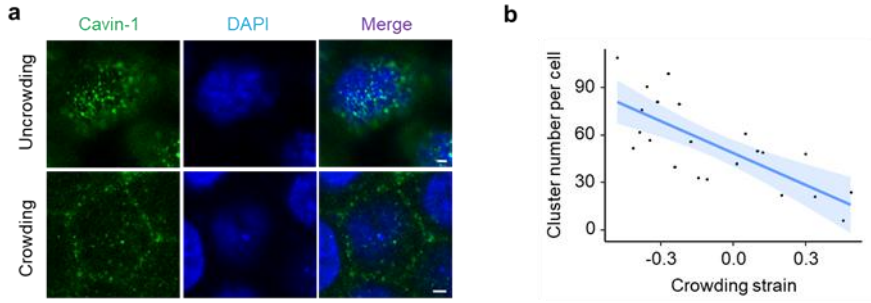

Fig. S4. The aggregation of Cavin-1 clusters at the apical membrane of crowded and uncrowded cells. (a) Representative XY confocal images showing immunostaining for Cavin-1 at the apical membrane of uncrowded and crowded HeLa cells. Scale bar: 2 μm. (b) Quantitation of correlation between the number of Cavin-1 clusters per cell and its crowding strain.

Fig. S5.

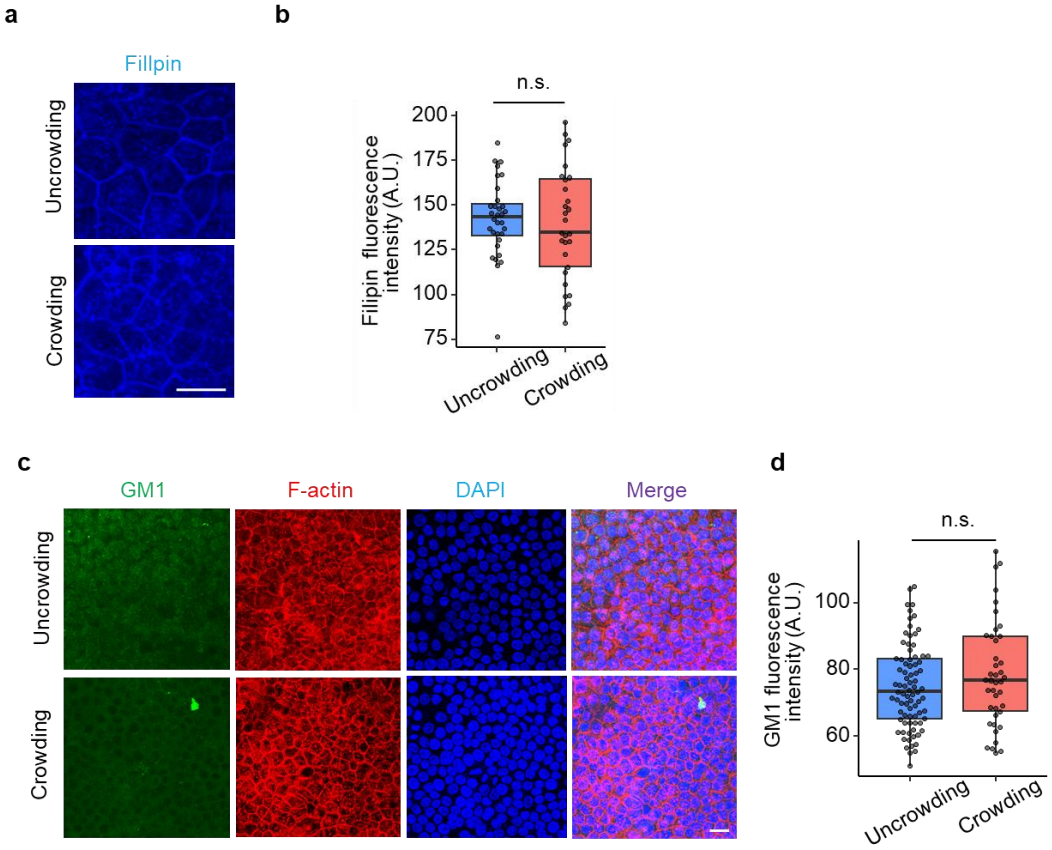

Fig. S5. Prolonged crowding does not affect the levels of main components within membrane doamins in cancer cells. (**a**) Representative XY confocal images showing filipin staining of cholesterol in different crowding regions of monoclonal HeLa cell sheet. Scale bar: 20 μm. (**b**) Quantitation of filipin fluorescence intensity in low and high crowding HeLa cells. (**c**) Representative XY confocal images showing immunostaining for GM1 in different crowding regions of monoclonal HeLa cell sheet. Scale bar: 20 μm. (**d**) Quantitation of GM1 fluorescence intensity in uncrowded and crowded HeLa cells. Data are presented as mean ± SEM. Data are presented as n.s., not significant; two-tailed unpaired t test.

Fig. S6.

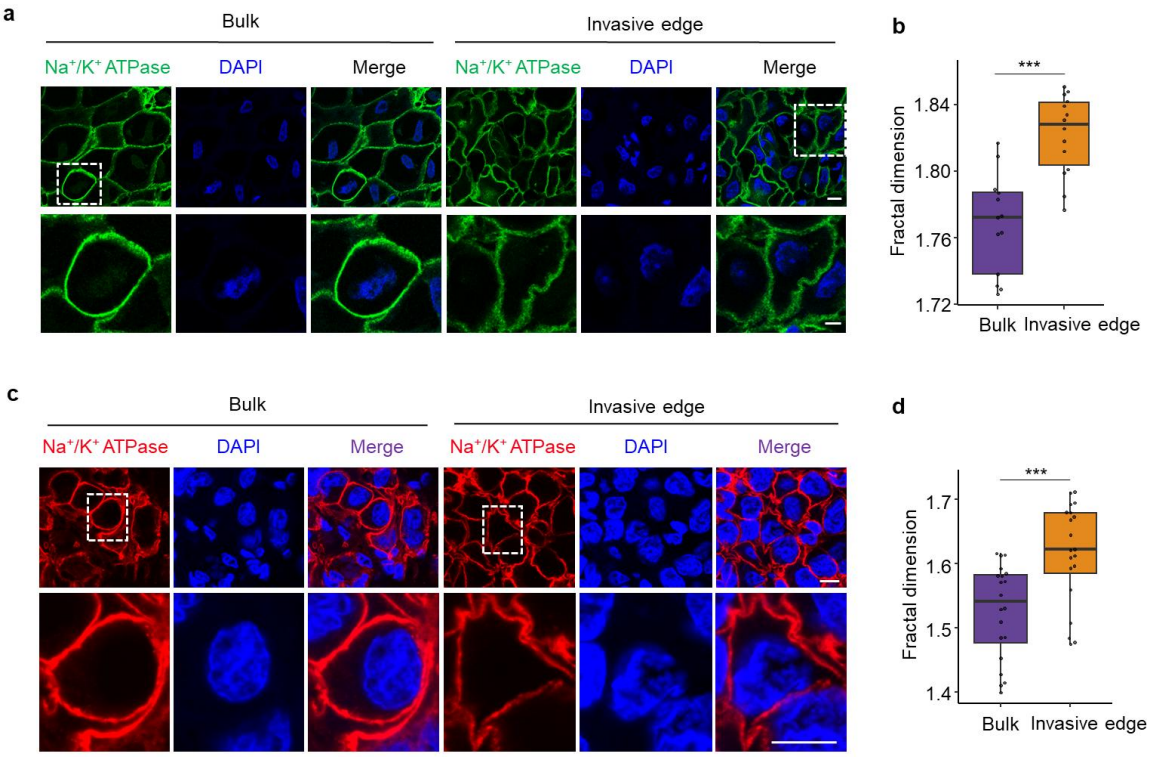

Fig. S6. Prolonged crowding triggers a nSCTT of plasma membranes in human tumor tissues. (**a**) Representative XY slice image of sodium potassium ATPase in the bulk and invasive edge of cervical cancer tissues. Scale bar: 10 μm. (**b**) Quantitation of correlation between fractal dimension per cell and its crowding strain in panel (a). (**c**) Representative XY slice image of sodium potassium ATPase in the bulk and invasive edge of breast cancer tissues. Scale bar: 10 μm. (**d**) Quantitation of correlation between fractal dimension per cell and its crowding strain in panel (c). Data are presented as mean ± SEM; ***$p < 0.005$; two-tailed unpaired t-test.

Fig. S7.

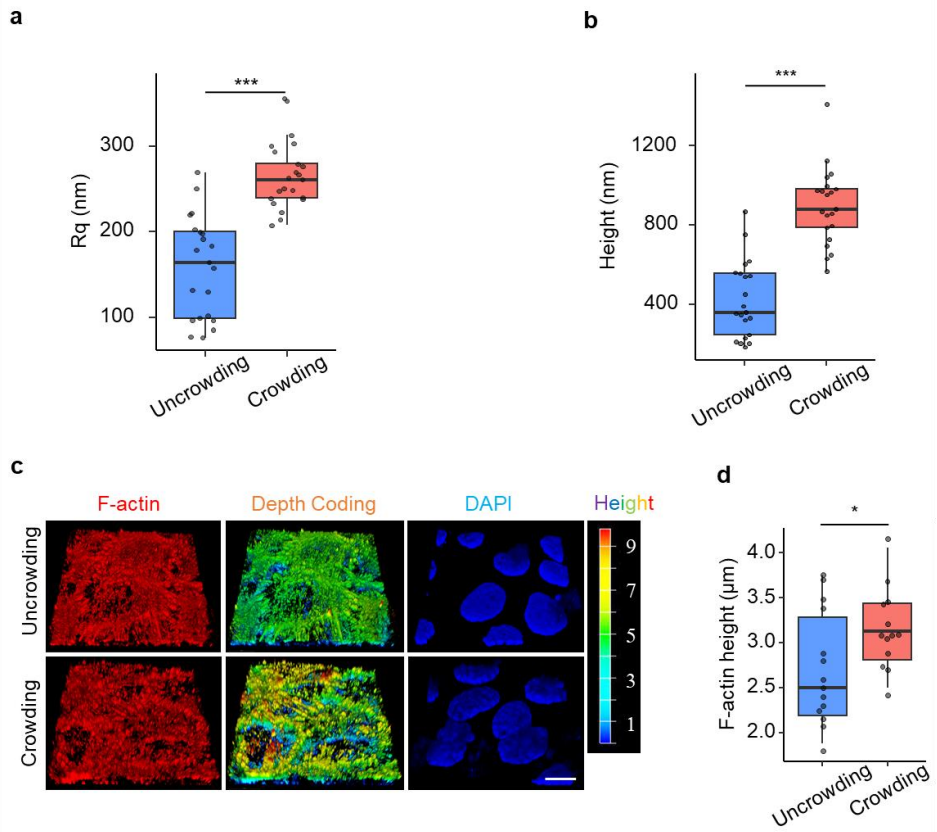

Fig. S7. Prolonged crowding triggers membrane protrusions and cortical actin remodeling. (**a**) Root-mean-squared roughness (Rq), and (**b**) height distribution were analyzed from 3×3 μm frame ultrastructure images of HeLa cells by AFM. (**c**) Confocal 3D reconstruction of F-actin at the apical membrane of uncrowded and crowded A431 cells. Scale bar: 10 μm. (**d**) Quantification of the average height of F-actin in uncrowded and crowded A431 cells in panel (c). Data are presented as mean±SEM; *$p < 0.05$, ***$p < 0.005$; two-tailed unpaired t-test.

Fig. S8.

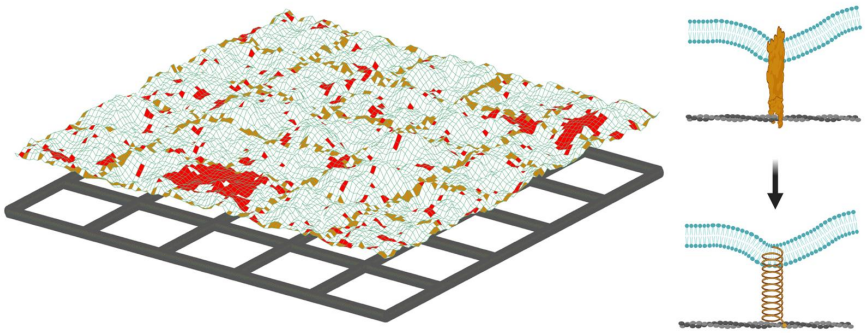

Fig. S8. Snapshot from Monte Carlo (MC) simulations of membrane-cortical actin system. Membranes are shown in blue, cortical actin in gray, membrane domains in red. Linker proteins are indicated by square patches in yellow. The membrane-cortical actin bonds were modeled as Hookean springs.

Fig. S9.

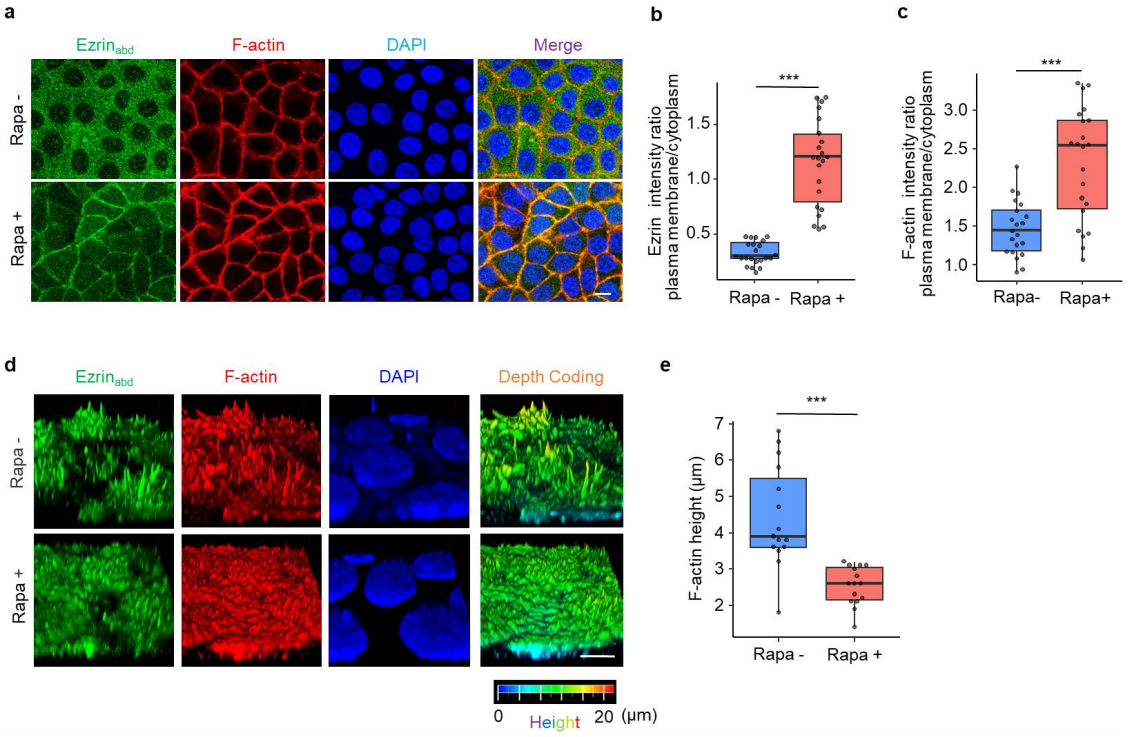

Fig. S9. Cortical actin remodeling in crowded cells is suppressed by enhancing MCA. (**a**) Immunofluorescence analysis of Ezrin$_{abd}$T567D in FKBP-Ezrin$_{abd}$T567D^{+} HeLa cells treated with rapamycin or vehicle. Scale bar: 10 μm. (**b**) Quantification of Ezrin$_{abd}$T567D intensity plasma membranes/cytoplasm ratio in panel (a). (**c**) Quantification of F-actin intensity plasma membranes/cytoplasm ratio in panel (a). (**d**) Confocal 3D reconstruction of F-actin at the apical membrane of FKBP-Ezrin$_{abd}$T567D^{+} HeLa cells treated with rapamycin or vehicle. Scale bar: 10 μm. (**e**) Quantification of the average height of F-actin in panel (d). Data are presented as mean ± SEM; ***$p < 0.005$; two-tailed unpaired t-test.

Fig. S10.

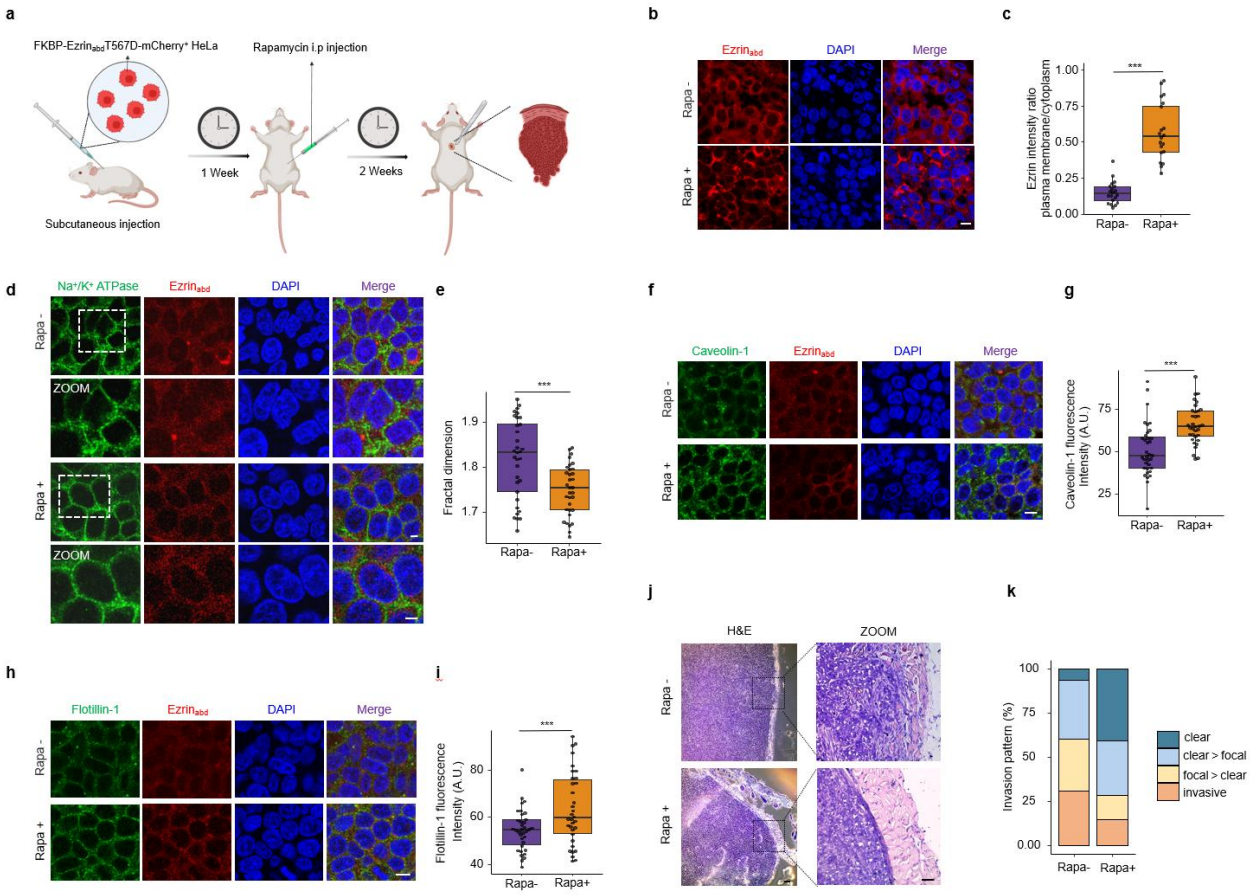

Fig. S10. Inhibiting the nSCTT of plasma membranes suppresses cancer cell invasiveness. (**a**) Schematic diagram of subcutaneous nude mouse xenograft model using FKBP-Ezrin$_{abd}$T567D^{+} HeLa cells. After 1 week of tumor growth, mice were treated with rapamycin or vehicle via i.p. three times per week. Tissues were harvested and tumor architectures were analyzed for the indicated parameters. (**b**) Immunofluorescence analysis of Ezrin$_{abd}$T567D in mouse xenografts treated with rapamycin or vehicle. Scale bar: 10 μm. (**c**) Quantification of Ezrin$_{abd}$T567D distribution in tumor cells of mouse xenografts. (**d**) Representative XY slice image of sodium potassium ATPase and Ezrin$_{abd}$T567D in mouse xenografts treated with rapamycin or vehicle. Scale bar: 5 μm. (**e**) Quantitation of fractal dimension per cell in panel (d). (**f**) Immunofluorescence analysis of Caveolin-1 in mouse xenografts treated with rapamycin or vehicle above. Scale bar: 10 μm. (**g**) Quantification of Caveolin-1 fluorescence intensity in panel (f). (**h**) Immunofluorescence analysis of Flotillin-1 in mouse xenografts treated with rapamycin or vehicle above. Scale bar: 10 μm. (**i**) Quantification of Flotillin-1 fluorescence intensity in panel (h). (**j**) Representative images of HE staining in mouse xenografts treated with rapamycin or vehicle. Overview images, scale bar: 200 μm; Detailed images, scale bar: 50 μm. (**k**) Invasion pattern of mouse subcutaneous xenografts treated with rapamycin or vehicle. The invasion was classified as “clear”, “clear>focal”, “focal>clear”, or “invasive”. Percentages of each category are given. Only samples with sufficient surrounding

`

1218 muscle tissue were evaluated. Schematic image (a) was created with BioRender.com. Data are
1219 presented as mean ± SEM; ***$p < 0.005$; two-tailed unpaired t-test.

`